

Copyright

by

Mark A. McEver

1999

Optimal Vibration Suppression Using On-line Pole/Zero Identification

by

Mark A. McEver, B.S.

Thesis submitted to the Faculty of the
Virginia Polytechnic Institute and State University
in partial fulfillment of the requirements for the degree of

Master of Science

in

Mechanical Engineering

Donald J. Leo, Chair
Harley H. Cudney
Daniel J. Inman

December 1999

Blacksburg, Virginia

Optimal Vibration Suppression Using On-line Pole/Zero Identification

Mark A. McEver, M.S.

Virginia Polytechnic Institute and State University, 1999

Advisor: Donald J. Leo

ABSTRACT

Vehicles and mechanisms which must perform very precise tasks or maneuvers require controllers to compensate for their inherent structural flexibility. Many of these applications involve structures that have time-varying dynamics, or have dynamics that are not considered in the traditional off-line controller design. These types of structures necessitate the use of adaptive control algorithms which can re-design themselves on-line in response to changes in the structural dynamics.

This work describes an on-line control algorithm that uses the pole-zero spacings of the collocated control-to-output transfer function to design the optimum Positive Position Feedback (PPF) control law. The PPF control law uses second-order filters to add closed-loop damping to resonant structural modes. An on-line PPF design algorithm was developed based on the theoretical model of the collocated control-to-output transfer function. The optimal PPF filter parameters are shown to be a function of the pole-zero spacing in the collocated transfer function. These parameters were found by solving the pole placement problem using a theoretical model for various pole-zero spacings. The parameters are then stored in a lookup table in the realtime controller, and a frequency sweep algorithm identifies the pole-zero spacing on-line and designs the PPF filters using the parameters in the lookup table.

A Phase-Locked Loop (PLL) was also studied as a means for adaptively tuning

the PPF filters on-line. The PLL behavior in the presence of random and deterministic signals was characterized. The PLL was used experimentally to tune a PPF filter to a changing modal frequency.

Analysis of the theoretical model indicated the amount of closed-loop damping a PPF filter can add monotonically increases with the amount of frequency spacing of the pole/zero pair. Experimental results with the on-line optimal PPF control algorithm proved it to be effective at adding damping to structures and suppressing vibration. The poles and zeros of the control-to-output transfer function were accurately identified by the pole/zero identification routine. However, the closed-loop performance was shown to be very dependent on the correct placement of sensor and actuator pairs. Tests with pointing control problems showed the algorithm to be better suited to vibration suppression rather than vibration isolation. Simulations and experiments with the phase-locked loop showed it to be unable to track a modal frequency of a structure excited by broadband noise. Bandpass prefilters would be necessary to eliminate the frequency content of the other modes, limiting the usefulness of the PLL.

**Optimal Vibration Suppression Using On-line
Pole/Zero Identification**

**Approved by
Advising Committee:**

Acknowledgments

First and foremost I would like to thank my advisor, Dr. Donald J. Leo for his wisdom and guidance throughout this process. Thanks go to my parents for their love and support during my years at Virginia Tech. Thanks also go to John Curtis for his friendship and for his LaTeX expertise.

The experimental work herein was supported by AFOSR Summer Extension Research Program as administered by Research and Development Laboratories, sub-contract 98-0810; and by the Mechanical Engineering Department of Virginia Tech. Thanks go to Kenn Newbury for his help with the plate experiment. Thanks go to Mr. Rory Nimmeman, our contact at AFRL Kirtland AFB, New Mexico. Many thanks go to Dr. Thomas Sharp of Sheet Dynamics, Ltd. for providing the SIMULINK RealTime Workshop interface to the MACE software.

MARK A. MCEVER

Virginia Polytechnic Institute and State University

December 1999

Contents

Abstract	iii
Acknowledgments	vi
List of Tables	x
List of Figures	xi
Chapter 1 Introduction	1
1.1 Motivation	1
1.2 Structural Control	3
1.3 Overview of Thesis	5
1.3.1 Contribution	5
1.3.2 Approach	6
Chapter 2 On-Line Positive Position Feedback Design Algorithm	7
2.1 Introduction	7
2.2 Basic Feedback Model	7
2.3 Positive Position Feedback	11
2.3.1 Optimal Closed-Loop Pole Locations	15
2.3.2 Optimal PPF Parameters	15
2.4 Simulation of the PPF Design Algorithm	22
2.4.1 Effect of Structural Damping on the Optimal Design	22
2.4.2 Effect of Multiple Modes on the Optimal Design	23

2.5	On-line Pole/Zero Identification Technique	25
2.5.1	Frequency Sweep Algorithm	25
2.5.2	Summary	30
Chapter 3 Phase-Locked Loop		32
3.1	Introduction	32
3.2	Detailed Model	32
3.3	Phase-Frequency Detector	36
3.4	Behavior of the PLL in the Presence of Noise	38
3.4.1	Random Signals	38
3.4.2	Deterministic Signals	40
3.5	Summary	45
Chapter 4 Experimental Results		46
4.1	Simply-Supported Plate	46
4.1.1	Test Setup	46
4.1.2	Results	48
4.2	MACE-II Experiment	53
4.2.1	Test Setup	53
4.2.2	Results - Phase-Locked Loop	54
4.2.3	Results - Optimal PPF Design	56
4.3	Mini-MACE	60
4.3.1	Test Setup	60
4.3.2	Results	61
4.4	Analysis of Payload Response	62
4.5	Summary	65
Chapter 5 Conclusions		67
5.1	Recommendations and Future Work	69
Bibliography		71

Appendix A	MATLAB code for optimal PPF design based on pole/zero spacing	73
Appendix B	MATLAB code to solve for optimal PPF parameters	75
Appendix C	MATLAB code to initialize control algorithm	77
Appendix D	SIMULINK diagram of digital phase-locked loop	82
Appendix E	SIMULINK diagram of frequency detector	83
Appendix F	SIMULINK diagram of on-line control algorithm	84
Appendix G	SIMULINK diagram of pole/zero identification routine	85
Appendix H	SIMULINK model of PPF filter	86
Appendix I	Mini-MACE schematics	87
Vita		90

List of Tables

3.1	Flip-flop output combinations and corresponding PFD state.	36
4.1	Results of experimental pole/zero identification on simply-supported plate.	49

List of Figures

1.1	Middeck Active Control Experiment (MACE) test article.	2
2.1	Two degree-of-freedom spring mass system.	8
2.2	Summation of first and second modes.	12
2.3	Typical collocated control-to-output frequency response.	13
2.4	Block diagram of controlled structure using Positive Position Feedback.	14
2.5	Root locus plot of controlled 2DOF spring-mass system: (a) pole/zero ratio of 2.41; (b) pole/zero ratio of 1.14; (c) pole/zero ratio of 1.14 with optimal PPF parameters	14
2.6	Optimal location of closed-loop poles.	16
2.7	Frequency response of undamped resonant system with $\omega_{pz} < 1$	21
2.8	Optimal PPF filter damping ratio as a function of the pole/zero spacing.	22
2.9	Closed-loop damping ratio as a function of the pole/zero spacing and gain margin, $\omega_{pz} > 1$	24
2.10	Closed-loop damping ratio as a function of the pole/zero spacing and gain, $\omega_{pz} < 1$	24
2.11	Closed-loop damping ratio difference between undamped and damped mode versus modal damping.	25
2.12	Two PPF filters in parallel.	26
2.13	First mode closed-loop damping ratio difference between the single mode case and the two mode case.	26
2.14	Bode plot of the closed-loop system with two modes and two PPF controllers, for various modal damping ratios.	27

2.15	Signal conditioning procedure for the pole/zero identification algorithm.	29
2.16	Frequency sweep to find pole/zero ratio, two zeros adjacent to pole. . .	29
3.1	Percent decrease in closed-loop damping ratio versus error of ω_f	33
3.2	Analog Phase-Locked Loop.	34
3.3	Phase-Frequency Detector.	35
3.4	State diagram for the PFD [Best (1984)].	37
3.5	Top figure: VCO signal, solid line; Input signal, dashed line. Bottom figure: PFD output.	38
3.6	3 Hz input signal to PLL with random noise.	39
3.7	VCO output of PLL.	39
3.8	Simulated step response of digital PLL with a PFD.	40
3.9	Signal-to-noise ratio required for lock versus noise frequency, digital PLL with Type-II PFD.	42
3.10	Signal-to-noise ratio required for lock versus noise frequency, analog PLL.	42
3.11	Simulation of digital PLL tracking ability with broadband excitation.	43
3.12	PLL output frequency from excitation of resonant system with 500 Hz noise.	43
3.13	(a) Time history of PLL input signal; (b) Power spectral density esti- mate of PLL input signal.	44
4.1	Simply-supported plate experiment.	47
4.2	Test setup and control architecture for plate experiment.	48
4.3	Frequency response of plate control-to-output transfer function. . . .	50
4.4	Frequency response of plate disturbance-to-output transfer function, 1st Mode PPF filter.	52
4.5	Frequency response of plate disturbance-to-output transfer function, 2nd Mode PPF filter.	52
4.6	Frequency response of plate disturbance-to-output transfer function, both PPF filters in parallel.	53

4.7	MACE-II primary gimbal.	54
4.8	PLL output frequency with 100 Hz bandwidth noise disturbance (PLL algorithm initialized at $t = 3$ sec).	55
4.9	Power spectral density estimate of sensor signal from broadband noise PLL test.	56
4.10	Block diagram of closed-loop system including performance variable. .	57
4.11	Experimental control-to-output transfer function.	58
4.12	Frequency response of disturbance-to-output using PPF controller designed with pole/zero algorithm.	59
4.13	Frequency response of disturbance-to-performance using PPF controller designed with pole/zero algorithm.	60
4.14	Mini-Mace test structure.	61
4.15	Closed-loop transient bus acceleration using PPF controller designed with pole/zero algorithm.	62
4.16	Closed-loop transient payload acceleration using PPF controller designed with pole/zero algorithm.	63
4.17	Spring-mass with pinned rod and mass.	64

Chapter 1

Introduction

1.1 Motivation

Due to the energy and cost constraints placed on launching payloads into orbit, engineers continue to design space structures with minimal mass and stiffness. While structural flexibility is not a great concern with most communication satellites, it imposes limitations on the performance of other space structures. Imaging satellites, space telescopes and military satellites must hold very precise positions or point instruments with very high line-of-sight accuracy, often while undergoing slewing or scanning maneuvers. Disturbance-induced vibrations limit the accuracy of these precision space structures, and their inherent flexibility exacerbates the problem. Without some sort of active structural control, these space structures are limited to performing maneuvers below the bandwidth of the flexible modes. Structural control is necessary to suppress vibration and therefore increase the operational bandwidth. However, many structures exhibit dynamics that vary with time, have different structural configurations, or have dynamics that differ in 0-gravity than experimental results in 1-gravity. Fixed-gain controllers are designed to compensate for one set of structural dynamics, and could be destabilized if the dynamics change significantly. Thus, for time-varying dynamics, an ideal control algorithm is one which can adapt to these changes and update itself in realtime.

The Middeck Active Control Experiment II (MACE-II) is an example of an ex-

periment designed to test adaptive structural control algorithms in 0-gravity aboard the International Space Station (ISS). The MACE-II test article simulates a spaceborne earth observing platform with multiple independent payloads. The control objective is to maintain inertial pointing of one payload while the other undergoes slewing or scanning motions. To test the performance of the adaptive control algorithms, the MACE-II test article can be assembled into four different structural configurations. Figure 1.1 shows the test article in configuration 1. MACE-II challenges the conventional control designer to develop adaptive control algorithms which can autonomously update themselves to handle the different configurations. The effects of zero gravity on the structural behavior are also important to consider in the control algorithm. Some of the experimental results in this work were obtained from ground tests of the MACE-II hardware at Kirtland AFB, Albuquerque, New Mexico.

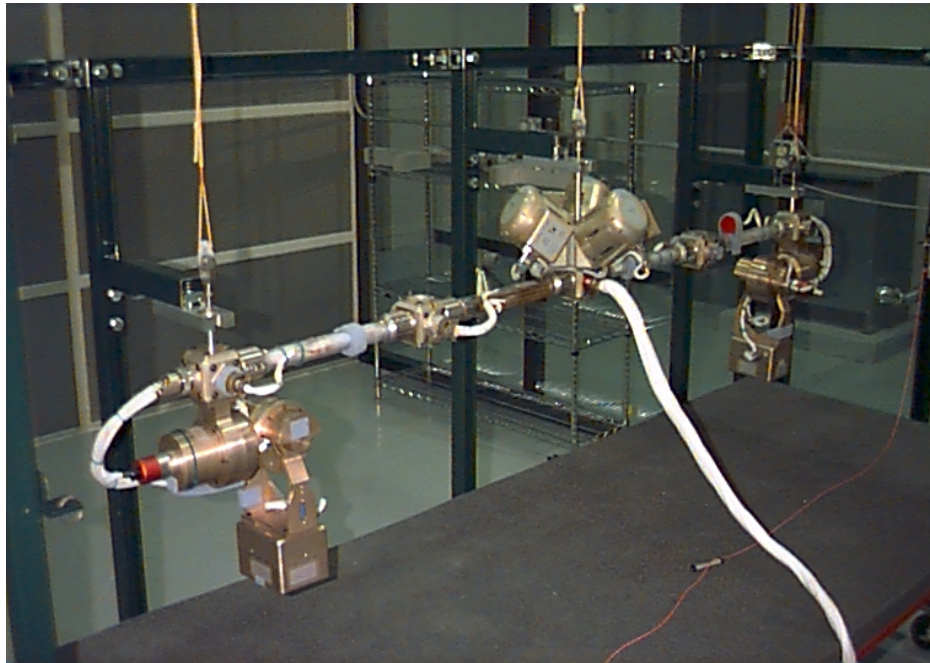


Figure 1.1: Middeck Active Control Experiment (MACE) test article.

1.2 Structural Control

There has been much research in the last thirty years on the subject of structural control. Prior to the space age, the theories of control were mainly applied to machinery and mechanisms. The proliferation of flexible spacecraft in the 1960's spawned a great deal of attention to the control of structural dynamics. The abrupt changes in magnitude and phase caused by structural resonances complicate the design of effective, stable controllers. Today, researchers continue to transition the theories of structural control into practical working systems.

Vibration suppression of flexible structures involving collocated actuators and sensors was discussed by Gevarter (1970) and Martin (1978), among others. Collocated control was shown to have simple stability criteria due to the alternating poles and zeros of the collocated transfer function. Miu and Yang (1994) showed the poles to be resonances of the structure, and the zeros to be resonances of the substructure constrained by the actuator and sensor. Proportional and velocity feedback control laws are globally stable because the phase of the control-to-output transfer function is bounded between 0° and -180° . This makes collocation of the actuator and sensor an attractive control approach.

Balas (1978) proposed many ideas for modern structural control. Balas analyzed a flexible system and described the two mechanisms for closed-loop instability: observation and control spillover. He described residual modes as dynamics that are not part of the mathematical model used for controller design. By eliminating the observation spillover from these residual modes, a stable control system can be achieved. Balas suggested using phase-locked loops (PLL) as narrow bandpass filters to remove the residual modes and eliminate observation spillover. He hypothesized that a PLL could also lock onto the actual modal frequency if the frequency is known imprecisely.

Positive Position Feedback (PPF) was first proposed by Fanson and Caughey (1990) as a feedback technique which is insensitive to finite actuator dynamics and can be made globally stable. PPF uses a second-order filter tuned to a particular mode targeted for control. Fanson and Caughey showed that the stability condition

does not depend on damping in the structure. They used PPF as a type of performance recovery for structures in which the collocated actuator and sensor caused close pole/zero spacings, without changing the location of the sensors or actuators.

Research by Dosch et al. (1995) used both PPF control and H_∞ control to add damping to the modes of a satellite antenna. PPF was shown to be just as effective as H_∞ , and was less sensitive to unmodeled high frequency dynamics. Dosch et al. also showed that one PPF filter may control more than one mode if the modes are closely spaced.

First-order PPF filters were used by Baz et al. (1992) to add damping to a beam with piezoceramic actuators and sensors. Modal displacements and velocities were computed on-line using modal filters. The computed modal displacement was fed into the PPF filter in a method called Independent Modal Space Control (IMSC). The optimal PPF filter time constants were determined off-line from the root locus of the loop transfer function.

Fagan (1993) did extensive research and experiments with implementing PPF filters in a digital controller to control vibration of a beam. Filter parameters were determined off-line from root locus plots of the analytical model. The model was updated with exact pole and zero frequencies from off-line experimental frequency response data. The effect of sampling period and discretization on the PPF filters was studied. Using the Tustin transformation, continuous filters were successfully mapped into the Z-plane.

Niezrecki and Cudney (1997) experimentally verified that a PLL could successfully prevent the instabilities of spillover. An analog PLL was used to lock onto the second mode of a cantilever beam and output a sinusoidal signal at that frequency. The output of the PLL was then fed to a piezoceramic actuator to add damping to the mode. The beam was excited by a tonal disturbance, and the PLL only operated when the disturbance frequency was within ± 15 Hz of the second mode. Niezrecki and Cudney also found problems with the PLL locking onto harmonics of the input signal. Other work involving PLLs include work by Davidson (1990) in which a similar algorithm called a frequency-locked loop was used to adaptively update a residual

mode filter.

A major motivation for this paper was a technique presented by Leo (1997) that used the output of a phase-locked loop to set the optimal parameters of a PPF controller on-line without a priori knowledge of the structure. The performance of a PPF control law depends on being accurately tuned to the mode. If the modal frequency changes significantly over time, the PPF filter must be redesigned. A frequency-tracking filter was designed using a frequency identification algorithm implemented with a phase-locked loop and a microcontroller. The first mode of a cantilever beam was varied between 24 Hz and 11 Hz by adding a tip mass. Experimental results showed that the adaptive filter could reliably track the natural frequency of the beam in approximately 500 microseconds and maintain between 14 percent and 20 percent damping [Leo and Griffin (1998)].

1.3 Overview of Thesis

1.3.1 Contribution

This thesis develops an on-line design algorithm for PPF filters based on pole-zero relationships in the collocated control-to-output transfer function. It also describes the effectiveness of the phase-locked loop in tracking changes in modal frequencies and tuning PPF filters. Optimal PPF filter parameters are developed based on analysis of a theoretical model of the control-to-output transfer function. These optimal parameters are then stored in a lookup table to design PPF filters on-line as a function of gain and pole/zero spacing. An on-line control algorithm is designed which identifies the pole/zero ratios and designs PPF filters from the parameters in the lookup table in realtime. A PLL algorithm is tested to track changes in modal frequencies and scale the PPF filter frequency accordingly. The advantages and disadvantages of using an on-line identification approach and a phase-locked loop approach are summarized, and recommendation for future research is given.

1.3.2 Approach

Chapter 2 describes the development of the optimal PPF filter design algorithm and the on-line pole/zero identification technique. Chapter 3 details the phase-locked loop and its behavior as a modal frequency-tracking device. Chapter 4 describes the experimental setup of the plate experiment, Mini-MACE, and MACE hardware and gives the experimental results. Finally, concluding remarks and recommendations for future work are given.

Chapter 2

On-Line Positive Position Feedback Design Algorithm

2.1 Introduction

This chapter develops a control algorithm using optimal PPF filters designed from on-line pole/zero identification. A theoretical model is analyzed to solve for the optimal PPF parameters as an explicit function of the pole/zero spacing in the collocated transfer function. An on-line routine is designed to identify the pole/zero frequency ratios and design optimal PPF filters from the optimal parameters. The effects of structural damping and the use of multiple PPF filters is discussed.

2.2 Basic Feedback Model

The structural modes of distributed-parameter systems can be modeled with the equations for a lumped mass multiple degree-of-freedom spring mass system. As an example, consider a structure where the first two modes are to be modeled. The two degree-of-freedom spring-mass system is shown below in Figure 2.1, with a control force f_c acting on mass 2 and a disturbance force f_d acting on mass 1.

The equation of motion for this system is:

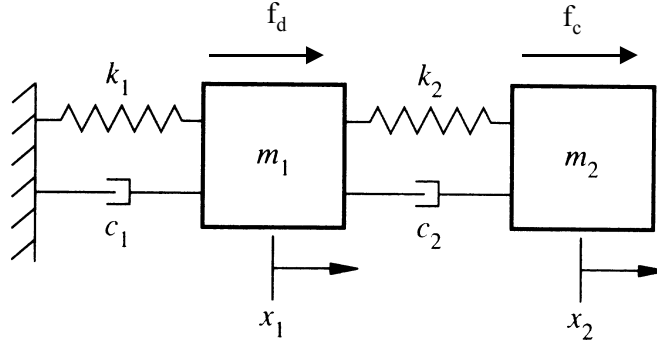


Figure 2.1: Two degree-of-freedom spring mass system.

$$M\ddot{\underline{x}} + C\dot{\underline{x}} + K\underline{x} = B_c f_c + B_d f_d \quad (2.1)$$

where $\underline{x} = \begin{bmatrix} x_1 \\ x_2 \end{bmatrix}$, $M = \begin{bmatrix} m_1 & 0 \\ 0 & m_2 \end{bmatrix}$, $K = \begin{bmatrix} k_1 + k_2 & -k_2 \\ -k_2 & k_2 \end{bmatrix}$,

$$B_c = \begin{bmatrix} 0 \\ 1 \end{bmatrix}, B_d = \begin{bmatrix} 1 \\ 0 \end{bmatrix}.$$

The damping matrix C can be written as a linear combination of the mass and stiffness matrices in order to allow modal decomposition [Inman (1996)]:

$$C = \alpha M + \beta K \quad (2.2)$$

where α and β are constants. This assumption is typically used when the structure has light damping ($\zeta < 0.01$). The influence matrices of the control force and the disturbance force are B_c and B_d , respectively. Using modal decomposition of the form

$$\underline{x} = \Phi \underline{\eta} \quad (2.3)$$

where the modal matrix is $\Phi = \begin{bmatrix} \phi_{11} & \phi_{12} \\ \phi_{21} & \phi_{22} \end{bmatrix}$, the vector of modal coordinates is

$\underline{\eta} = \begin{bmatrix} \eta_1 \\ \eta_2 \end{bmatrix}$, the total response of each physical coordinate x_1 and x_2 can be written as a sum of the individual contributions of each mode. This allows the transformation of the coupled equations of motion in equation (2.1) into the decoupled equations of [Inman (1996)]

$$\ddot{\underline{\eta}} + \Delta \dot{\underline{\eta}} + \Omega \underline{\eta} = \Phi^T B_c f_c + \Phi^T B_d f_d \quad (2.4)$$

$$\text{where } \Delta = \begin{bmatrix} 2\zeta_1\omega_1 & 0 \\ 0 & 2\zeta_2\omega_2 \end{bmatrix}, \text{ and } \Omega = \begin{bmatrix} \omega_1^2 & 0 \\ 0 & \omega_2^2 \end{bmatrix}.$$

Applying the Laplace transform to equation (2.4) yields a set of transfer functions of the disturbance and control forces to each modal coordinate:

1st Mode

$$\eta_1(s) = \frac{\begin{bmatrix} \phi_{21} & \phi_{11} \end{bmatrix} \begin{bmatrix} f_c(s) \\ f_d(s) \end{bmatrix}}{s^2 + 2\zeta_1\omega_1 s + \omega_1^2} \quad (2.5)$$

2nd Mode

$$\eta_2(s) = \frac{\begin{bmatrix} \phi_{22} & \phi_{12} \end{bmatrix} \begin{bmatrix} f_c(s) \\ f_d(s) \end{bmatrix}}{s^2 + 2\zeta_2\omega_2 s + \omega_2^2} \quad (2.6)$$

As can be seen in equations (2.5) and (2.6), the modal matrix elements give insight into the modal participation of the control and disturbance forces.

Consider the two degree-of-freedom spring mass system again. Let the control objective be to minimize the motion of the second mass in the presence of the disturbance force on the first mass. Let the sensed output y be the displacement of the

second mass x_2 . Thus the control force and output sensor are spatially collocated, and using equations (2.3), (2.5) and (2.6) the control-to-output transfer function can be written as

$$y = x_2 = \phi_{21}\eta_1 + \phi_{22}\eta_2$$

$$\frac{y(s)}{f_c(s)} = \frac{(\phi_{21}^2 + \phi_{22}^2)s^2 + (2\phi_{21}^2\zeta_2\omega_2 + 2\phi_{22}^2\zeta_1\omega_1)s + \phi_{21}^2\omega_2^2 + \phi_{22}^2\omega_1^2}{(s^2 + 2\zeta_1\omega_1s + \omega_1^2)(s^2 + 2\zeta_2\omega_2s + \omega_2^2)} \quad (2.7)$$

In the same manner the disturbance-to-output transfer function can be written

$$\frac{y(s)}{f_d(s)} = \frac{(\phi_{21}\phi_{11} + \phi_{22}\phi_{12})s^2 + (2\phi_{21}\phi_{11}\zeta_2\omega_2 + 2\phi_{22}\phi_{12}\zeta_1\omega_1)s + \phi_{21}\phi_{11}\omega_2^2 + \phi_{22}\phi_{12}\omega_1^2}{(s^2 + 2\zeta_1\omega_1s + \omega_1^2)(s^2 + 2\zeta_2\omega_2s + \omega_2^2)} \quad (2.8)$$

For analysis of the relationships between different parameters of the structure, it is helpful to transform the transfer functions from functions of the Laplace operator s to functions of nondimensional frequency σ , where $s = j\omega_1\sigma$, and to introduce ω_{21} , the ratio of the second modal frequency to the first:

$$\frac{y(\sigma)}{f_c(\sigma)} = \frac{-(\phi_{21}^2 + \phi_{22}^2)\sigma^2 + (2\phi_{21}^2\zeta_2\omega_{21} + 2\phi_{22}^2\zeta_1)j\sigma + \phi_{21}^2\omega_{21}^2 + \phi_{22}^2}{(-\sigma^2 + 2\zeta_1j\sigma + 1)(-\sigma^2 + 2\zeta_2\omega_{21}j\sigma + \omega_{21}^2)} \quad (2.9)$$

$$\frac{y(\sigma)}{f_d(\sigma)} = \frac{(\phi_{21}\phi_{11} + \phi_{22}\phi_{12})\sigma^2 + (2\phi_{21}\phi_{11}\zeta_2\omega_{21} + 2\phi_{22}\phi_{12}\zeta_1)j\sigma + \phi_{21}\phi_{11}\omega_{21}^2 + \phi_{22}\phi_{12}}{(-\sigma^2 + 2\zeta_1j\sigma + 1)(-\sigma^2 + 2\zeta_2\omega_{21}j\sigma + \omega_{21}^2)} \quad (2.10)$$

In Multiple Input Multiple Output (MIMO) systems, occasionally the performance variable measured by one sensor is different than the output variable used in the feedback loop. Denoting the performance variable z , the input-output relationships for a controlled structure can be described by the set of open-loop transfer functions:

$$\begin{bmatrix} z(\sigma) \\ y(\sigma) \end{bmatrix} = \begin{bmatrix} G_{zc}(\sigma) & G_{zd}(\sigma) \\ G_{yc}(\sigma) & G_{yd}(\sigma) \end{bmatrix} \begin{bmatrix} f_c(\sigma) \\ f_d(\sigma) \end{bmatrix} \quad (2.11)$$

where G_{yc} is the control-to-output transfer function, G_{zc} is the control-to-performance transfer function, G_{yd} is the disturbance-to-output transfer function, and G_{zd} is the disturbance-to-performance transfer function. Looking at G_{yc} in equation (2.7), there will be zero output when the driving frequency ($s = j\omega$) causes the numerator to be zero. At this frequency, the physical displacement of the mass is zero because the modal displacements of the first and second mode are equal in amplitude but 180° out of phase, hence they sum to zero (see Figure 2.2). The frequency response of a typical collocated control-to-output transfer function is shown in Figure 2.3. An alternating pole/zero (modal resonance/anti-resonance) structure like this is characteristic of a collocated actuator/sensor pair. It will be proved later that the maximum amount of damping a PPF controller can add to a particular mode is a function of the pole/zero spacing in that frequency band. If the structure has no damping, it is simple to find the frequency at which the zero occurs by setting the numerator of equation (2.9) to zero:

$$\sigma_{zero} = \sqrt{\frac{\phi_{21}^2 \omega_{21}^2 + \phi_{22}^2}{\phi_{21}^2 + \phi_{22}^2}} \quad (2.12)$$

Since $s = j\omega_1\sigma$, and at the zero frequency $s = j\omega_z$, we can write

$$\sigma_{zero} = \omega_{z1} = \frac{\omega_z}{\omega_1} \quad (2.13)$$

where ω_{z1} is the ratio of the zero frequency to the first mode frequency.

2.3 Positive Position Feedback

Positive Position Feedback (PPF) feeds the sensed position through a filter with second-order dynamics and sends the resulting signal to the control actuator [Fanson and Caughey (1990)]. The benefits are in its simplicity and its effectiveness at

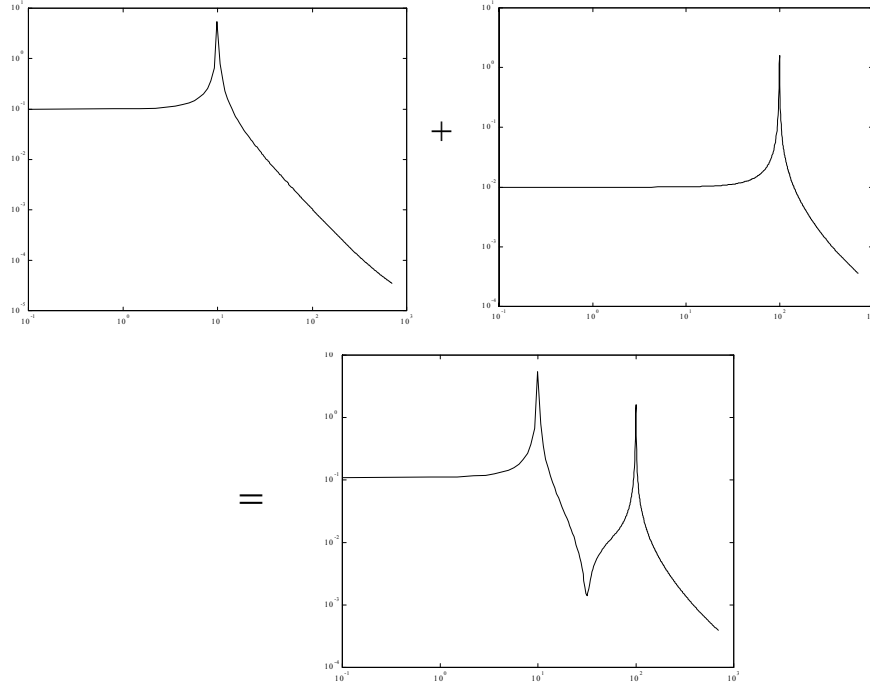


Figure 2.2: Summation of first and second modes.

adding damping to resonant modes. PPF is also very suitable for use with collocated actuator/sensor pairs. The transfer function for the PPF filter is:

$$G_{PPF}(s) = \frac{g\omega_f^2}{s^2 + 2\zeta_f\omega_f s + \omega_f^2} \quad (2.14)$$

where g is the filter gain, ζ_f is the filter damping ratio, and ω_f is the filter frequency. Figure 2.4 shows a block diagram of the controlled structure with a PPF filter placed in the feedback loop.

Using a second-order PPF filter in the feedback loop adds another set of poles to the resulting closed-loop system. Figure 2.5a shows the root locus plot as a function of gain for the two degree-of-freedom undamped spring mass system with a PPF feedback control law. The nondimensional parameter ω_{21} was set to 3 for all three cases. For the simulation in Figure 2.5a, ϕ_{21} and ϕ_{22} were set to 0.1 and 0.08 respectively, which yielded a pole/zero spacing of $\omega_{z1} = 2.41$.

The PPF filter is being used to add damping to the first mode. As the PPF filter gain is increased, the pole at the first mode (undamped) moves away from its location

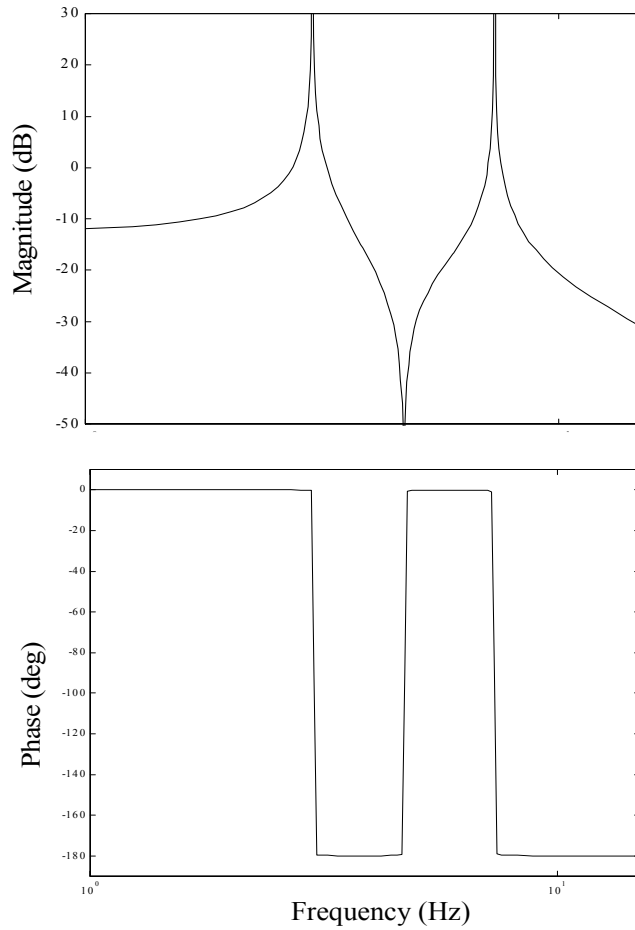


Figure 2.3: Typical collocated control-to-output frequency response.

on the imaginary axis and becomes more damped. Notice the location of the zero on the imaginary axis with respect to the pole corresponding to the second mode. For the next simulation in Figure 2.5b, ϕ_{21} and ϕ_{22} were set to 0.1 and 0.5 respectively, which yielded a pole/zero spacing of $\omega_{z1} = 1.14$. Notice that the maximum damping that the PPF controller adds is 50% less when the pole/zero spacing is decreased. This is consistent with the fact that less pole/zero spacing approaches pole/zero cancelation, and causes the actuator to have less control authority. However, the parameters for the PPF controller were kept constant for both simulations. If the PPF damping ratio ζ_f is decreased and the PPF frequency ω_f is increased, then the damping performance is recovered as shown in Figure 2.5c. In general, there will be one set of PPF filter parameters that will yield the optimal closed-loop pole locations

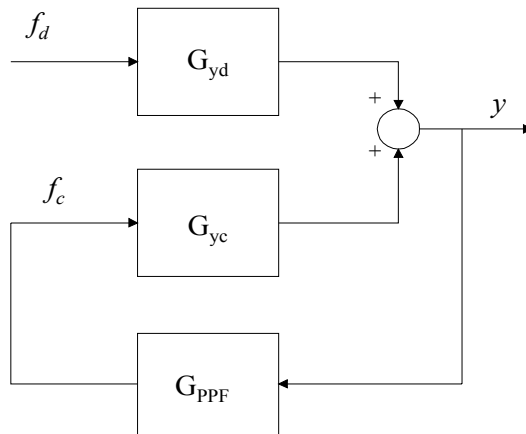


Figure 2.4: Block diagram of controlled structure using Positive Position Feedback.

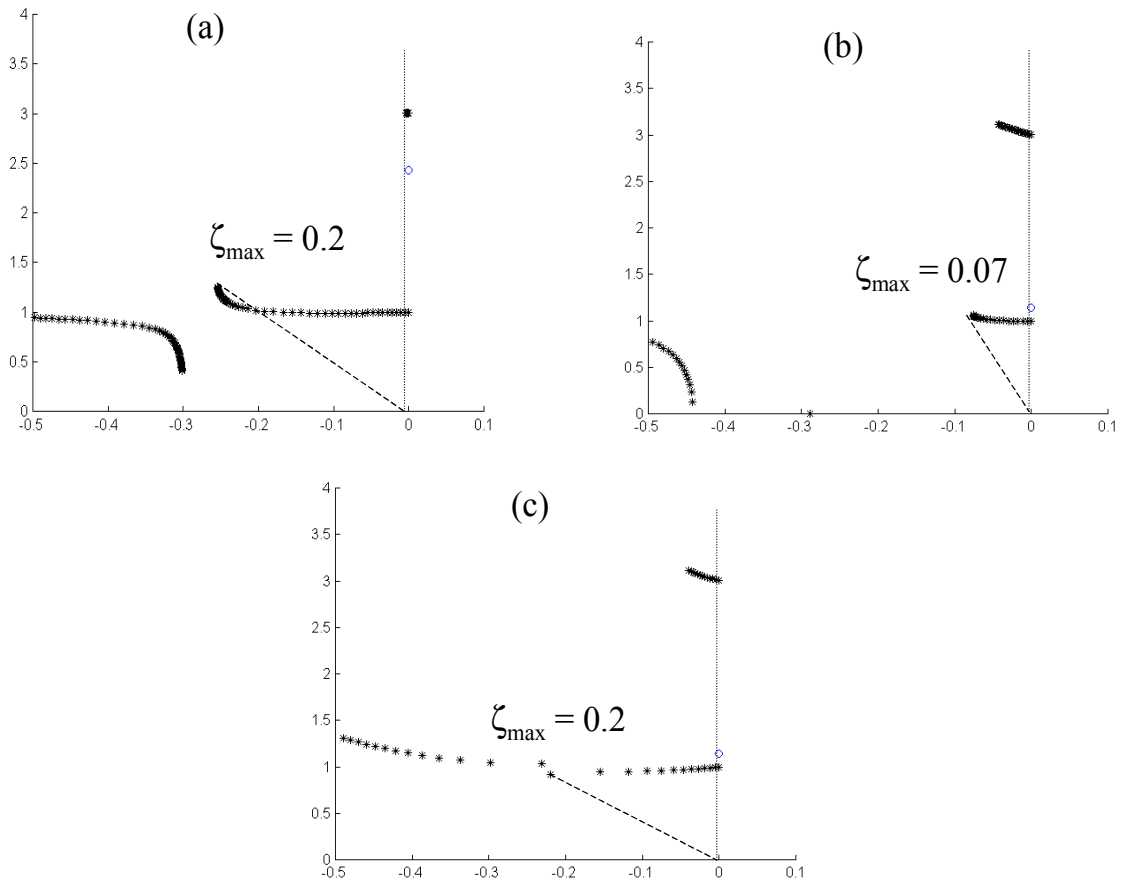


Figure 2.5: Root locus plot of controlled 2DOF spring-mass system: (a) pole/zero ratio of 2.41; (b) pole/zero ratio of 1.14; (c) pole/zero ratio of 1.14 with optimal PPF parameters

with maximum closed loop damping ζ_{CL} . The optimal locations will be defined in the next section. The maximum amount of closed-loop damping that can be added by a PPF controller is a function of the pole/zero spacing and the PPF parameters:

$$\zeta_{CL} = f(g, \zeta_f, \omega_f, \omega_{pz}) \quad (2.15)$$

where ω_{pz} is the ratio of the zero frequency to the pole frequency, $\frac{\omega_z}{\omega_p}$. The following section defines the optimal closed-loop pole locations.

2.3.1 Optimal Closed-Loop Pole Locations

With the PPF filter, the goal is to place the closed-loop poles in an ‘optimal’ location in the complex plane, *i.e.* have optimal values of damping and frequency. As mentioned previously, there will be two pairs of closed-loop poles to place because the PPF filter adds additional dynamics. For this particular pole placement problem optimal is defined with respect to maximizing damping, and is the location where both resulting closed-loop poles have an equal damping ratio. Figure 2.6 shows the optimal closed-loop pole locations. From the law of similar triangles, the second closed-loop pole frequency is some multiple α of the first pole’s frequency or

$$\omega_2 = \alpha\omega_1 \quad (2.16)$$

2.3.2 Optimal PPF Parameters

The goal for the on-line PPF design algorithm is to use the optimal PPF filter to add damping to resonant structural modes, given a particular pole/zero spacing in G_{yc} . To find the optimal PPF parameters, it is helpful to look at the simplest case where G_{yc} has one undamped pole followed by one undamped zero, and G_{yd} has simply one pole:

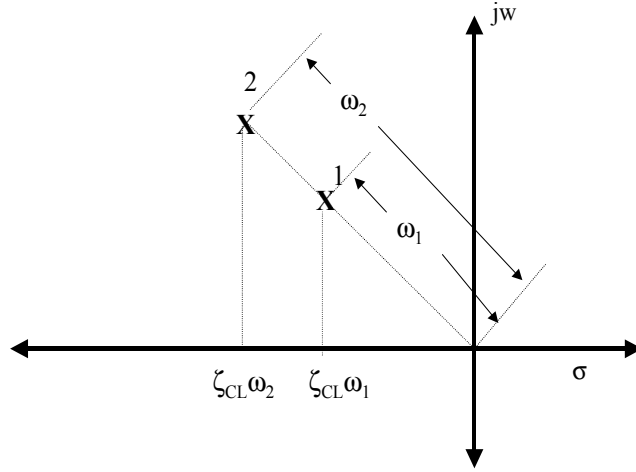


Figure 2.6: Optimal location of closed-loop poles.

$$G_{yc}(s) = \frac{s^2 + \omega_z^2}{s^2 + \omega_p^2}$$

and

$$G_{yd}(s) = \frac{1}{s^2 + \omega_p^2} \quad (2.17)$$

It is helpful to transform these equations into functions of nondimensional frequency σ by substituting $s = j\omega_p\sigma$:

$$G_{yc}(\sigma) = \frac{\omega_{pz}^2 - \sigma^2}{\sigma^2 - 1}$$

and

$$G_{yd}(\sigma) = \frac{1}{-\sigma^2\omega_p^2 + \omega_p^2} \quad (2.18)$$

where ω_{pz} is the ratio of the zero to the pole, $\frac{\omega_z}{\omega_p}$. Since we are using a PPF filter for control, we need to nondimensionalize its equations as well:

$$G_{PPF}(\sigma) = \frac{-g\omega_{fp}^2}{\sigma^2 - 2\zeta_f\omega_{fp}j\sigma - \omega_{fp}^2} \quad (2.19)$$

where ω_{fp} is the ratio of the PPF filter frequency to the pole frequency, $\frac{\omega_f}{\omega_p}$.

Referring back to the block diagram of the closed-loop controlled structure in Figure 2.4, the closed-loop transfer function will be

$$G_{CL}(\sigma) = \frac{G_{yd}(\sigma)}{1 - G_{PPF}(\sigma)G_{yc}(\sigma)} \quad (2.20)$$

Substitution of equations (2.18) and (2.19) into equation (2.20) yields the closed-loop characteristic equation:

$$C.L.C.E. = \sigma^4 - (2\zeta_f\omega_{fp}j)\sigma^3 + [\omega_{fp}^2(1 - g) - 1]\sigma^2 + (2\zeta_f\omega_{fp}j)\sigma + \omega_{fp}^2(1 - g\omega_{pz}^2) \quad (2.21)$$

Using the optimal closed-loop pole locations in Figure 2.6, we can write another form of the closed-loop characteristic equation:

$$C.L.C.E. = (s^2 + 2\zeta_{CL}\omega_1s + \omega_1^2)(s^2 + 2\zeta_{CL}\alpha\omega_1s + \alpha^2\omega_1^2) \quad (2.22)$$

Factoring equation (2.22) and transforming into a function of nondimensional frequency σ yields

$$\begin{aligned} C.L.C.E. = \sigma^4 - j2\zeta_{CL}\frac{\omega_1}{\omega_p}(\alpha + 1)\sigma^3 - \left(\frac{\omega_1}{\omega_p}\right)^2(\alpha^2 + 4\zeta_{CL}^2\alpha + 1)\sigma^2 \\ + j2\zeta_{CL}\left(\frac{\omega_1}{\omega_p}\right)^3(\alpha^2 + \alpha)\sigma + \left(\frac{\omega_1}{\omega_p}\right)^4\alpha^2 \end{aligned} \quad (2.23)$$

With both forms of the closed-loop equation, we can now perform pole placement by equating equation (2.21) and (2.23). This yields four equations:

$$\zeta_{CL} \frac{\omega_1}{\omega_p} (\alpha + 1) = \zeta_f \omega_{fp} \quad (2.24)$$

$$\left(\frac{\omega_1}{\omega_p}\right)^2 (\alpha^2 + 4\zeta_{CL}^2 \alpha + 1) = \omega_{fp}^2 (1 - g) + 1 \quad (2.25)$$

$$\zeta_{CL} \left(\frac{\omega_1}{\omega_p}\right)^3 (\alpha^2 + \alpha) = \zeta_f \omega_{fp} \quad (2.26)$$

$$\left(\frac{\omega_1}{\omega_p}\right)^4 \alpha^2 = \omega_{fp}^2 (1 - g \omega_{pz}^2) \quad (2.27)$$

Noting that the left side of equation (2.24) must equal the left side of equation (2.26), we can write $\frac{\omega_1}{\omega_p}$ as a function of α :

$$\frac{\omega_1}{\omega_p} = \sqrt{\frac{1}{\alpha}} \quad (2.28)$$

Substituting $\sqrt{\frac{1}{\alpha}}$ for $\frac{\omega_1}{\omega_p}$ in equations (2.24), (2.25), and (2.28) yields three equations that can be used to solve for the optimal PPF parameters:

$$\zeta_{CL} \left(\frac{1}{\sqrt{\alpha}} + \sqrt{\alpha}\right) = \zeta_f \omega_{fp} \quad (2.29)$$

$$\alpha + 4\zeta_{CL}^2 + \frac{1}{\alpha} = \omega_{fp}^2 (1 - g) + 1 \quad (2.30)$$

$$\omega_{fp}^2 (1 - g \omega_{pz}^2) = 1 \quad (2.31)$$

With the previous three equations we can solve for the optimal PPF parameters ζ_f and ω_{fp} by choosing the filter gain g and the closed-loop pole spacing α . Given a particular ω_{pz} , and choosing g , we can solve for ω_{fp} from equation (2.31):

$$\omega_{fp} = \sqrt{\frac{1}{1 - g\omega_{pz}^2}} \quad (2.32)$$

Substituting equation (2.32) into equation (2.30) yields the closed-loop damping ζ_{CL} as a function of the pole/zero spacing ω_{pz} and the closed-loop pole spacing α :

$$\zeta_{CL} = \frac{1}{4} \sqrt{\frac{1 - g}{1 - g\omega_{pz}^2} + 1 - \alpha - \frac{1}{\alpha}} \quad (2.33)$$

It is obvious from equation (2.33) that choosing $\alpha = 1$ will yield the maximum ζ_{CL} . The relationship between the closed-loop damping ratio and the pole/zero spacing can now be clarified by examining the stability of the closed-loop system. Because we are using positive feedback, instability will occur when the open-loop phase is $0^\circ \pm m360^\circ$, $m = 1, 2, 3, \dots$. With a collocated control-to-output transfer function, this will occur at zero frequency (static instability). The open-loop transfer function G_{OL} is the PPF filter in series with G_{yc} or

$$G_{OL}(s) = \left(\frac{g\omega_f^2}{s^2 + 2\zeta_f\omega_f s + \omega_f^2} \right) \left(\frac{s^2 + \omega_z^2}{s^2 + \omega_p^2} \right) \quad (2.34)$$

Substituting $s = 0$ into equation (2.34) we find that the DC magnitude of G_{OL} is $g\omega_{pz}^2$, thus for stability $g < \frac{1}{\omega_{pz}^2}$. The gain margin is then defined as

$$GM = \frac{1}{g\omega_{pz}^2} \quad (2.35)$$

Substitution of the expression in equation (2.35) into equation (2.33) with $\alpha = 1$, we now have a more general expression for the closed-loop damping as a function of the pole/zero spacing:

$$\zeta_{CL} = \frac{1}{4} \sqrt{\frac{1 - \frac{1}{GM\omega_{pz}^2}}{1 - GM^{-1}} - 1} \quad (2.36)$$

For any gain margin GM , we have proved that the closed-loop damping ratio ζ_{CL} increases monotonically with an increase in the pole/zero spacing ω_{pz} . This verifies analytically that decreasing the pole/zero spacing decreases the amount of damping a PPF controller can add to the mode, and that at exact pole/zero cancelation ($\omega_{pz} = 1$) the closed-loop damping is 0. This also shows that the amount of closed-loop damping is inversely proportional to the gain margin, because high gain gives the controller more authority over the mode.

From looking at equation (2.36), if the pole/zero ratio is less than one the resulting closed-loop damping ratio will be a complex number. If the pole/zero ratio is less than one, the PPF filter gain needs to be negative in order to yield a real solution. There is no physical basis for this; rather, it is due to the theoretical model only containing one zero and one pole. If the zero occurs before the pole, its phase at low frequency is 0° , rises to 180° due to the zero, then falls back to 0° . A negative gain is necessary to bring the phase of the open-loop transfer function back down to -180° . This is not necessary in an actual structure, because the collocated transfer function will always start with a pole (the first mode) and the phase around the zero will be -180° .

To continue the solution of the optimal PPF parameters, we now calculate the closed-loop damping ratio from equation (2.36) and use it to calculate the required PPF filter damping ratio:

$$\zeta_f = \frac{2\zeta_{CL}}{\omega_{fp}} \quad (2.37)$$

To summarize, the optimal PPF parameters solution is:

1. Choose PPF filter gain g , positive if $\omega_{pz} > 1$, negative if $\omega_{pz} < 1$.
2. Calculate ω_{fp} from equation (2.31).
3. Choose the closed-loop pole spacing α to be 1.
4. Calculate the closed-loop damping ratio ζ_{CL} from equation (2.30).

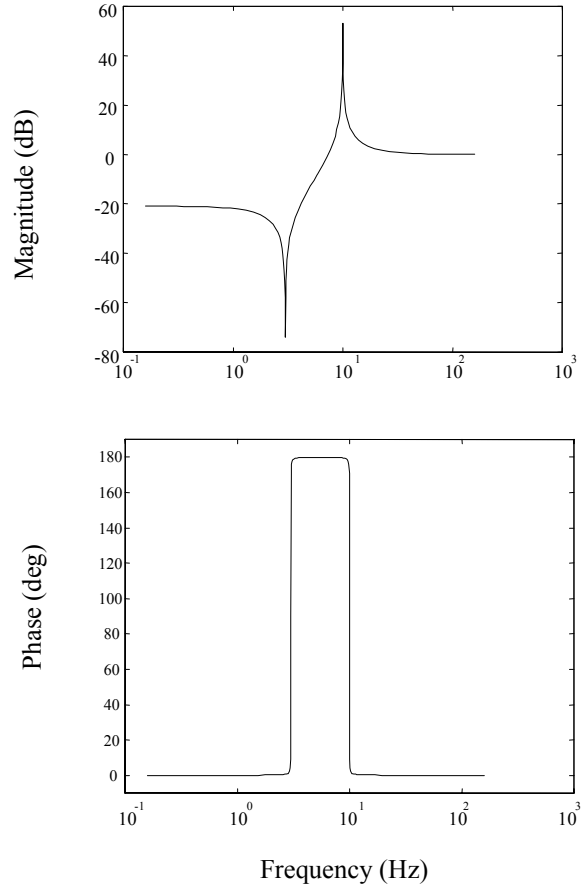


Figure 2.7: Frequency response of undamped resonant system with $\omega_{pz} < 1$.

5. Calculate the required PPF filter damping ratio ζ_f from equation (2.29).

By solving these equations and finding the optimal PPF parameters for various pole/zero spacings off-line, the on-line design algorithm can simply identify the pole/zero spacing in the bandwidth of interest, then find the proper PPF parameters for that pole/zero spacing from a lookup table. This requires very little computational time of the digital controller. Figure 2.8 shows the optimal PPF damping ratio ζ_f as a function of the pole/zero spacing using a gain margin of 2.

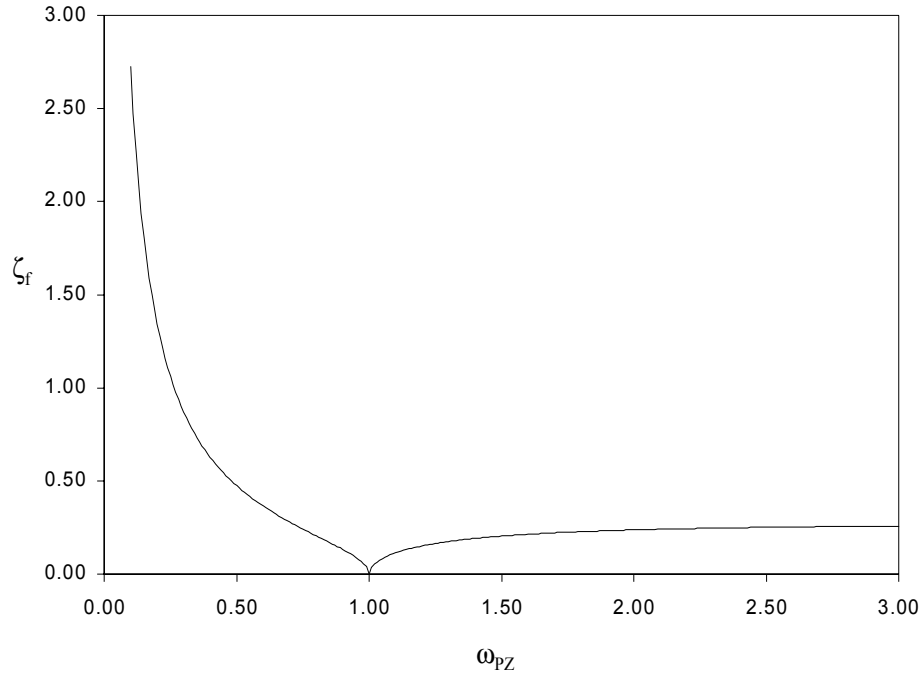


Figure 2.8: Optimal PPF filter damping ratio as a function of the pole/zero spacing.

2.4 Simulation of the PPF Design Algorithm

2.4.1 Effect of Structural Damping on the Optimal Design

Figures 2.9 and 2.10 show the closed-loop damping ratio as a function of the pole/zero spacing and the PPF filter gain. As previously stated, the amount of closed-loop damping the PPF filter can add is zero when $\omega_{pz} = 1$, and increases to approximately 80% critical damping for high gain. Even with a comfortable gain margin of 2, if the pole/zero ratio is at least 1.5, then PPF can add 40% damping. However, the PPF parameters were solved using a theoretical model with no open-loop damping in the mode. To study the effect of modal damping on the performance of the PPF controller, a simulation was performed using the same PPF filters designed in the undamped case but controlling a structure with damping in the mode. Figure 2.11 shows the percent difference of the closed-loop damping ratios in the damped and undamped case. Since the equations used to solve for the PPF parameters neglect

extra terms that would be present with modal damping, the closed-loop roots will not be in the optimal location as designed with pole placement. However Figure 2.11 shows that the closed-loop poles will still be damped to within a few percent of the optimal damping.

2.4.2 Effect of Multiple Modes on the Optimal Design

To add damping to multiple modes, traditional PPF control laws use a PPF filter per mode unless the modes are close enough in frequency to fall in the bandwidth of the controller. The multiple PPF filters are connected in parallel in the feedback path as shown in Figure 2.12.

The optimal PPF parameters were solved using a single PPF filter. However, the on-line PPF design algorithm can be used to design multiple PPF filters on a mode-by-mode basis. Due to the rolloff dynamics of the PPF filter, lower frequency PPF controllers will not affect higher frequency controllers, but higher frequency controllers can destabilize lower frequency controllers. This problem can be alleviated by adjusting the DC gains of the individual PPF filters to provide the necessary gain margin at low frequency. To test the ability of the optimal design algorithm to handle multiple PPF filters, the theoretical model was modified to include a second mode and zero. The closed-loop system was simulated with the second mode at various frequencies to test the effect of the second mode PPF controller on the performance on the first mode PPF controller. Figure 2.13 shows the difference in the closed-loop damping in the first mode between the single mode case and the two mode case. As can be seen, the second mode controller only changes the damping in the first mode by a few percent. Independent multiple PPF design using the pole/zero algorithm is possible without degrading the performance of each individual controller.

Figure 2.14 shows the Bode plot of the closed-loop system with two modes and two PPF controllers for damping ratios between 0 and 0.1.

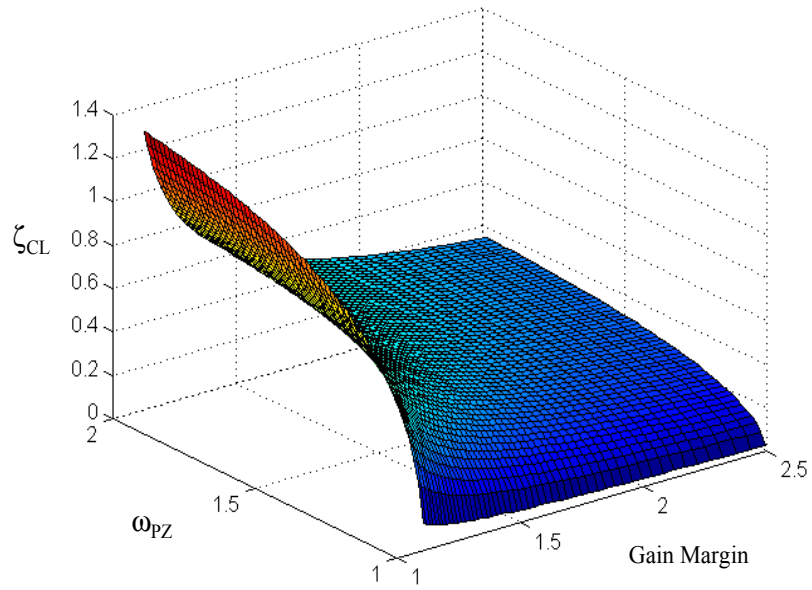


Figure 2.9: Closed-loop damping ratio as a function of the pole/zero spacing and gain margin, $\omega_{pz} > 1$.

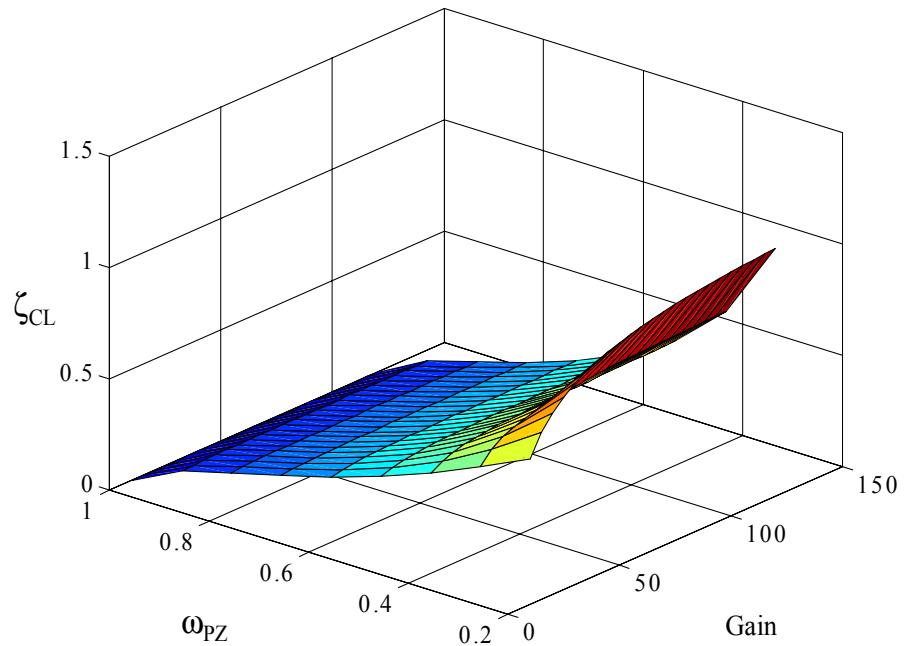


Figure 2.10: Closed-loop damping ratio as a function of the pole/zero spacing and gain, $\omega_{pz} < 1$.

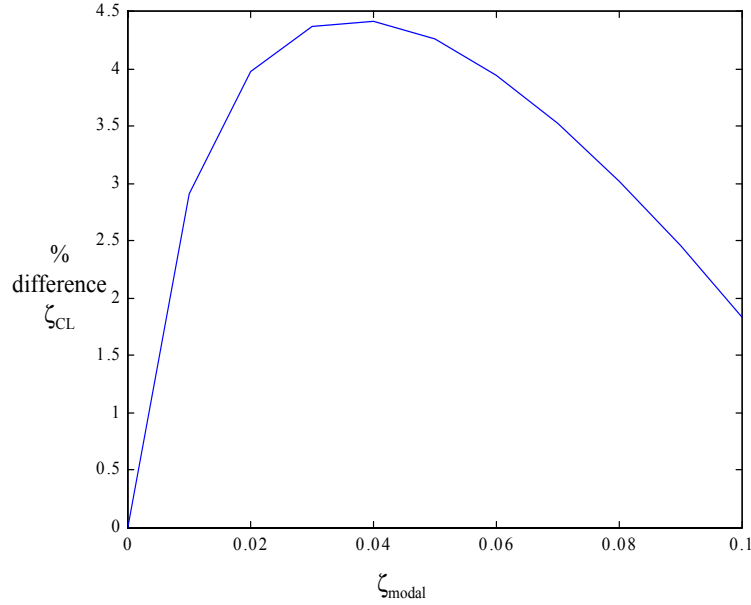


Figure 2.11: Closed-loop damping ratio difference between undamped and damped mode versus modal damping.

2.5 On-line Pole/Zero Identification Technique

2.5.1 Frequency Sweep Algorithm

In order to design the PPF controllers in realtime using the pole/zero algorithm, the algorithm must identify the pole/zero spacing in the collocated G_{yc} transfer function. To accomplish this, a frequency sweep algorithm was designed which determines the pole/zero spacing from the collocated sensor output. A sinusoidal chirp signal is sent to the control actuator, and the sensor signal is fed into the pole/zero identification routine. The chirp signal starts from a low frequency and increases in frequency to the ending frequency according to

$$\omega_{chirp}(t) = \left(\frac{\omega_{end} - \omega_{start}}{t_{end}^2} \right) t^2 + \omega_{start} \quad (2.38)$$

where ω_{chirp} is the chirp frequency, ω_{start} is the starting frequency, ω_{end} is the ending frequency, and t_{end} is the total time for the sweep. The chirp frequency is a quadratic function of time to dwell longer at lower frequencies than higher frequencies. This

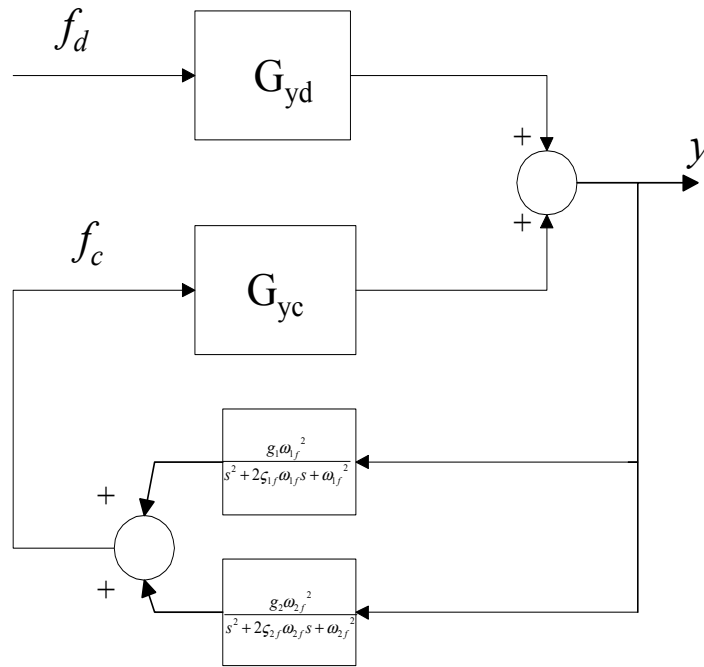


Figure 2.12: Two PPF filters in parallel.

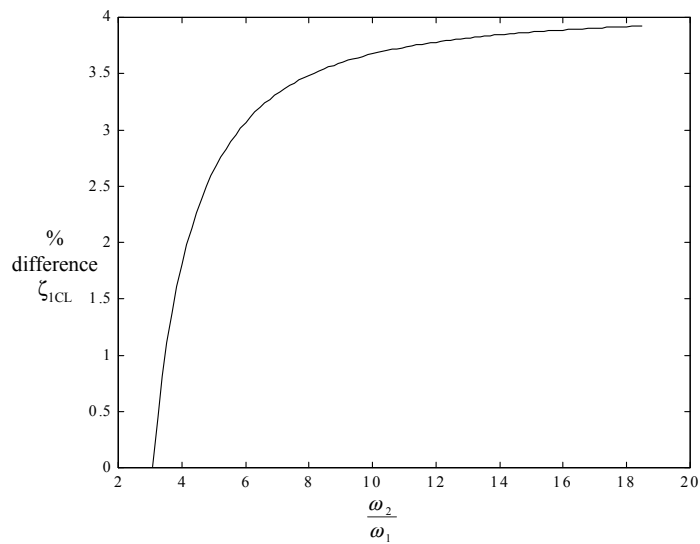


Figure 2.13: First mode closed-loop damping ratio difference between the single mode case and the two mode case.

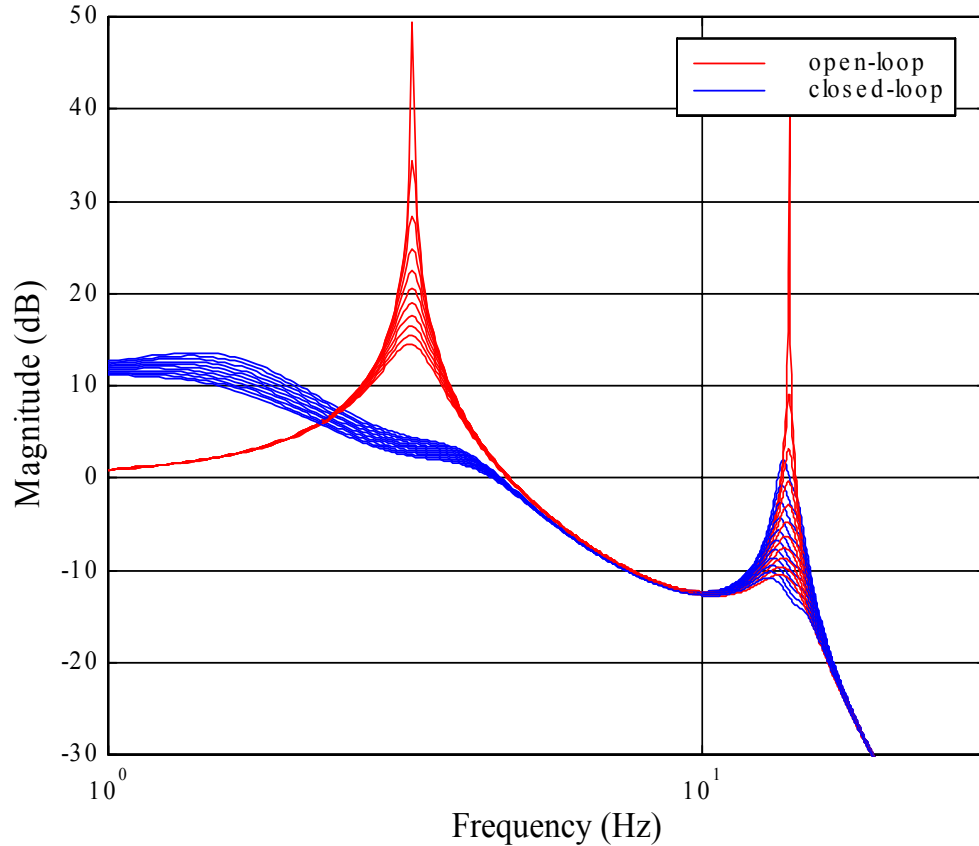


Figure 2.14: Bode plot of the closed-loop system with two modes and two PPF controllers, for various modal damping ratios.

helps the identification routine because the number of cycles at the lower frequencies is almost as much as the number of cycles at higher frequencies. It also allows time for the transient response to decay.

Figure 2.15 shows the flowchart for the signal conditioning of the sensor signal. The signal from the output sensor is filtered with a filter containing a zero at zero frequency to eliminate any DC offset. The zero-biased signal is then rectified by taking its absolute value. The rectified signal is filtered by a second-order lowpass filter to attenuate the double frequency component and reduce spurious noise. The filter has a cutoff frequency proportional to the bandwidth of the frequency sweep, and a damping ratio of 0.707 for an optimally flat frequency response. To find the pole, it is assumed

that the approximate modal frequency is known within the bandwidth of the starting and ending frequencies, but the exact modal frequency is unknown. The pole/zero identification algorithm is initialized with the starting and ending frequency of the sweep, which correspond to the frequency bounds that the pole/zero pair is known to be within. The pole identification routine is simply a running maximum loop which finds the peak response during the sweep, and then calculates the frequency at that peak response from equation (2.38). After finding the pole frequency, the sweep is repeated to find the zero frequency with a running minimum loop. The running minimum is reset when the sweep passes through the pole frequency, should there be zeros above and below the pole frequency. In that case, the zero closest to the pole is recorded and that pole/zero ratio is used to find the optimal PPF parameters from the lookup table. Figure 2.16 illustrates the pole/zero identification routine when there are two zeros adjacent to the pole.

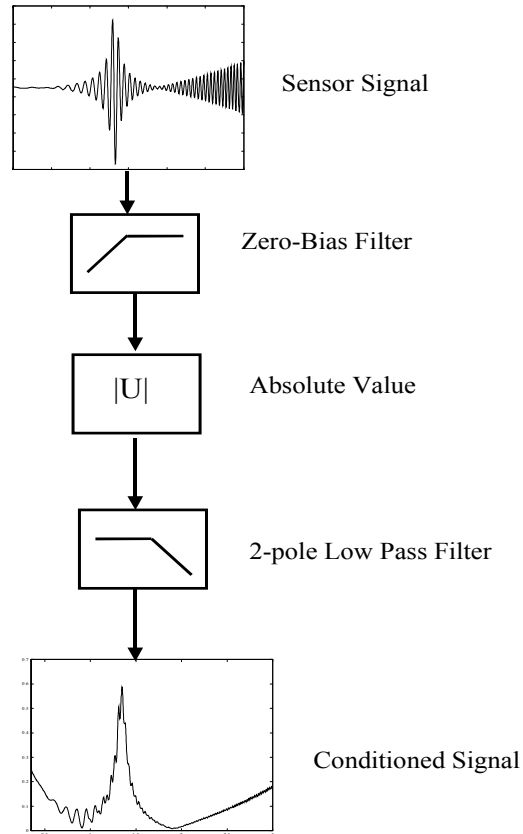


Figure 2.15: Signal conditioning procedure for the pole/zero identification algorithm.

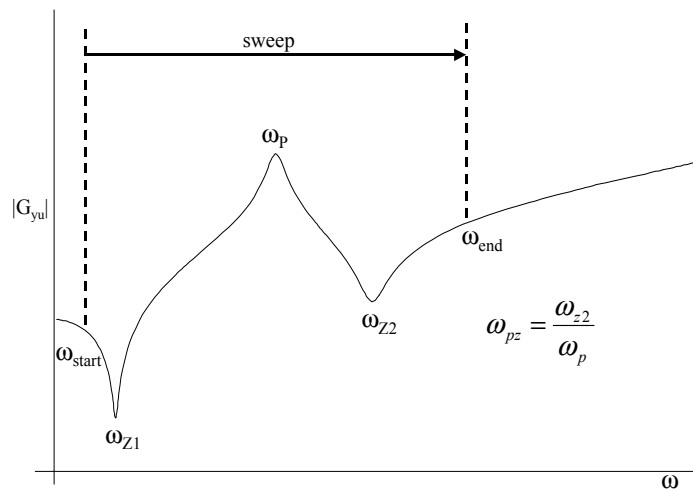


Figure 2.16: Frequency sweep to find pole/zero ratio, two zeros adjacent to pole.

With the solution of the optimal PPF parameters as a function of the pole/zero spacing, a lookup table containing these parameters can be used in the realtime control algorithm. After identifying the pole and zero frequencies, the PPF filters can be designed from the parameters in the lookup table. Assuming that the disturbance is inactive during the identification procedure, the complete on-line control algorithm is as follows:

1. Excite structure with control actuator
2. Measure collocated sensor output
3. Find pole and zero frequencies with pole/zero identification algorithm
4. Design optimal PPF filters from lookup table
5. Start control

There are many advantages of this type of algorithm. It is not significantly dependent on the mathematical model of the structure. Because it identifies the pole and zero frequencies on-line, it uses the most recent experimental data available. However, the algorithm is not completely autonomous; it cannot detect changes in the structural dynamics once it has performed the pole/zero identification. For a structure with multiple configurations like the MACE-II test article, the algorithm would need to be performed for each configuration.

2.5.2 Summary

A model containing an undamped pole and zero of the collocated actuator-to-sensor transfer function was studied. Optimal closed-loop pole locations were defined, and the pole placement problem was solved to find the optimal PPF filter parameters. A control algorithm was developed which identifies the pole/zero spacing on-line and designs PPF filters from a lookup table containing the optimal PPF parameters. Even though the optimal parameters were found from an undamped model, they were still effective at adding closed-loop damping to structures already having damping. A

theoretical model including multiple modes was also studied. A PPF filter for each mode was designed with the optimal algorithm, and the PPF filters were connected in parallel in the feedback path. The performance of the first mode PPF filter in both the single and multiple mode case was found to be similar. The main conclusions that can be drawn from this analysis are as follows:

1. The maximum closed-loop damping ratio achievable is proportional to the frequency spacing of the collocated pole/zero pair.
2. Structural damping has a negligible effect on the damping performance of the optimal PPF filter.
3. Independent PPF design is possible for multi-mode control.

Chapter 3

Phase-Locked Loop

3.1 Introduction

The ability of PPF controllers to add damping to structural modes is highly dependent on proper tuning of the control parameters. Significant deviations of the modal frequency can detune a fixed-parameter PPF controller [Leo and Griffin (1998)]. Figure 3.1 shows the results of a simulation using the same controlled two degree-of-freedom spring mass system in Section 2.2, but with the PPF filter detuned. As can be seen, only a 5 percent difference between the optimal and actual PPF filter frequency results in the damping being decreased by as much as 30 percent. For structures with variable mass, the modes targeted for control can shift in frequency and detune the PPF controllers. For this reason, phase-locked loops were investigated as a means to track the modal frequency and scale the PPF filter frequency accordingly, without a complete redesign of the controller.

3.2 Detailed Model

Used widely in electronics, the phase-locked loop is a frequency-tracking device that matches its own frequency to that of the input frequency. It acts on the phase difference between the input signal and a reference signal to adjust its oscillator frequency. All PLL's have three common components: a phase detector, a loop filter,

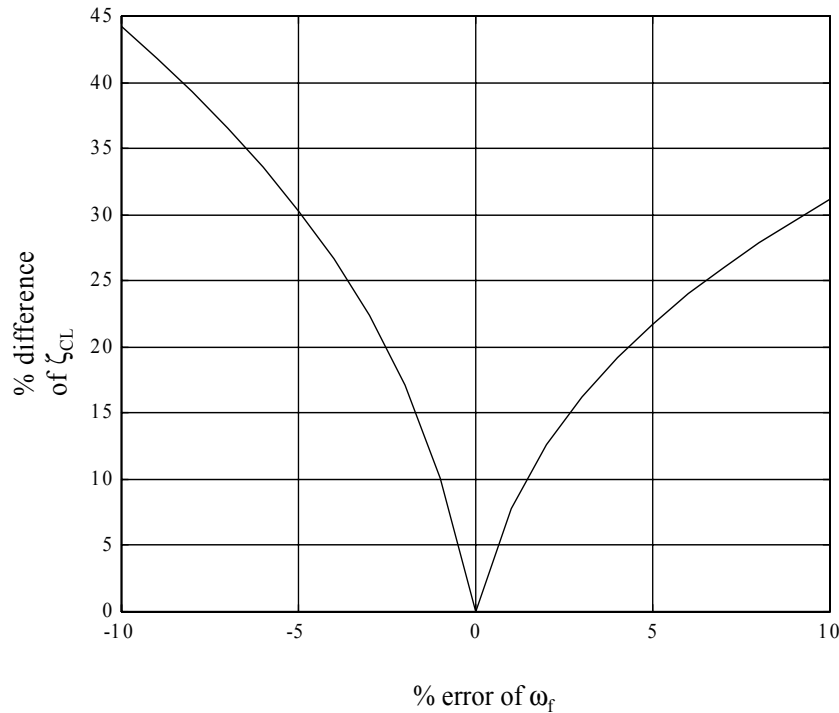


Figure 3.1: Percent decrease in closed-loop damping ratio versus error of ω_f .

and a voltage-controlled oscillator (VCO). The two main parameters that characterize the performance of PLL's are:

1. $\Delta\omega_H$ Hold Range - frequency range within which the PLL is statically stable
2. $\Delta\omega_C$ Capture Range - maximum initial frequency difference of the input signal and the VCO signal for which the PLL can still obtain lock

To understand how a PLL obtains lock it is easier to first understand the simplest analog PLL (see Figure 3.2). The phase detector takes the input signal containing the frequency of interest and compares its phase to the output signal of the VCO. In the most basic phase detectors, this involves analog multiplication of the two signals. Let the input signal to the PLL be $u_{in}(t) = A \sin(\omega_{in}t + \Theta_{in}(t))$ and the output of the VCO be $u_{VCO}(t) = B \sin(\omega_{VCO}t + \Theta_{VCO}(t))$. Then the output of the phase detector is the product of the two signals or

$$u_{in}(t)u_{VCO}(t) = \frac{1}{2}AB[\sin(\omega_{in}t - \omega_{VCO}t + \Theta_{in}\Theta_{VCO}) + \sin(\omega_{in}t - \omega_{VCO}t + \Theta_{in}\Theta_{VCO})] \quad (3.1)$$

As can be seen in equation (3.1), when the VCO frequency approaches the input frequency ($\omega_{VCO} \approx \omega_{in}$), the output of the phase detector is the superposition of an AC signal and a DC offset proportional to the phase difference of the VCO signal and the input signal [Best (1984)]. The loop filter is typically a first-order low-pass filter designed to attenuate the AC component and pass the DC offset to the VCO.

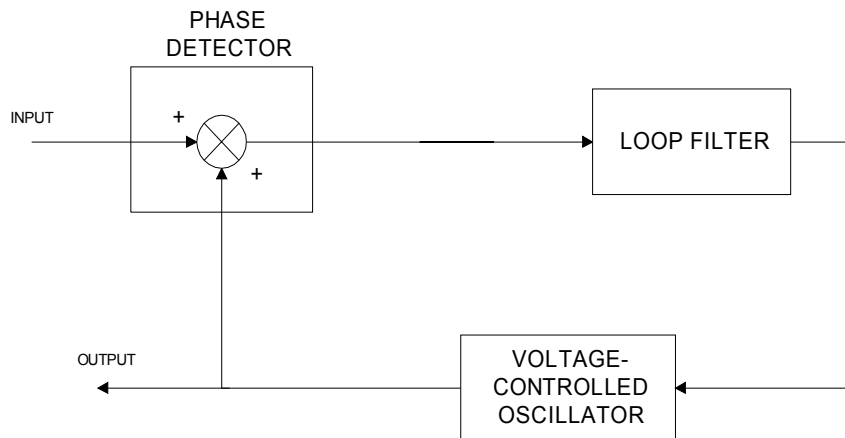


Figure 3.2: Analog Phase-Locked Loop.

The VCO is a device that outputs a signal with a frequency proportional to its DC input voltage. The DC offset is fed back into the VCO and changes the operating frequency of the VCO. Notice that this is a simple feedback loop that minimizes the error between the phase of the VCO and the input signal, hence locking the VCO

output onto the input signal. For analog PLLs using a multiplying phase detector, the loop filter time constant is inversely proportional to the capture range, so the loop filter can be used to set the capture range [Best (1984)].

In this work, a digital PLL implemented in software was simulated and tested on a real-time processor. Digital PLLs are characterized by the type of phase detector used to compare the reference signal to the input signal. Type I phase detectors are based on an exclusive-OR logic gate and behave like analog multipliers. Type II phase detectors are also called phase-frequency detectors (PFD) because they operate on both the phase difference and the frequency difference of the two signals. The PFD algorithm used in this paper is from MATLAB's Communications Toolbox SIMULINK© library and is shown in Figure 3.3. It is based on the Type-II PFD.

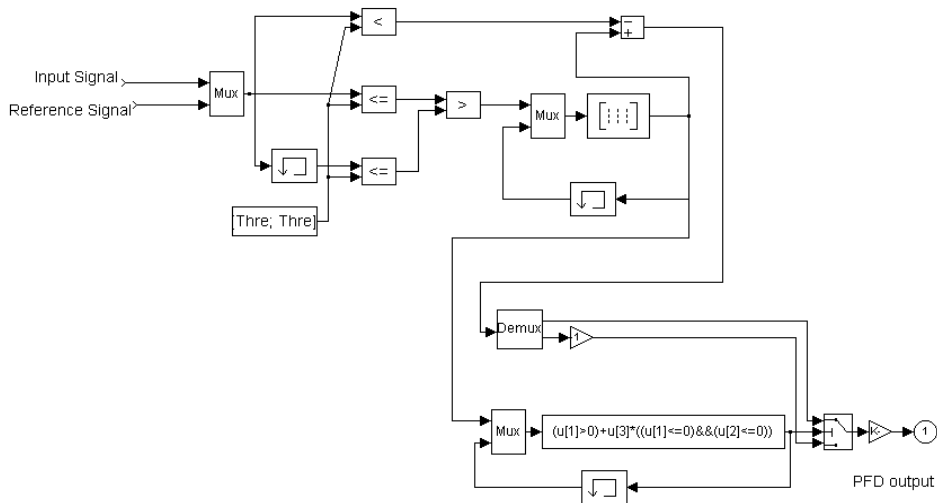


Figure 3.3: Phase-Frequency Detector.

3.3 Phase-Frequency Detector

The PFD acts on the rising edges of the input signal and the reference signal produced by the VCO. This technique is called the zero crossing technique, because the PFD output depends on the relative timing of the zero crossings of the input signal. The right half of the PFD diagram shows the algorithm that changes the state of the PFD, called a flip-flop because its behavior is analogous with the JK flip-flop integrated circuit. The flip-flop outputs logic high (+1) when one input crosses from positive to negative, and outputs logic low (0) when its other input crosses positive to negative. Table 3.1 shows the output combinations of the flip-flops and the corresponding state of the PFD.

Table 3.1: Flip-flop output combinations and corresponding PFD state.

Flip-flop Output 1	Flip-flop Output 2	PFD State
1	0	-1
0	0	0
1	0	+1

Figure 3.4 contains a diagram showing what events cause the PFD to change its state. If the input signal is initially higher in frequency than the VCO frequency, then it generates more positive transitions per unit of time than the VCO signal. Looking at Figure 3.5, the PFD will only stay between the states 0 and +1 under this condition. If the input signal were less than the VCO frequency, then the PFD would stay between -1 and 0. It can be then be concluded that the PFD varies its output with respect to the frequency error $\omega_{in} - \omega_{VCO}$ [Best (1984)].

A PLL using a PFD as its phase detector will perform better than one with a type-I detector because the PFD uses the initial frequency difference to track in the direction of the input, then uses the phase difference to lock onto the input. However, a PLL using a PFD also has an infinite capture range because the PFD output tracks the VCO towards the input frequency irrespective of the initial difference. As will be discussed later, this will present difficulties when there are other signals at higher

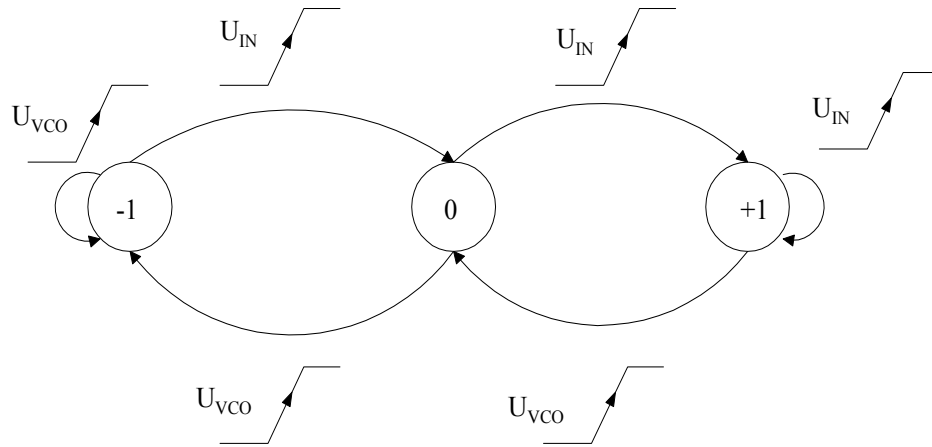


Figure 3.4: State diagram for the PFD [Best (1984)].

frequencies present in the input signal.

To visualize the process of locking onto a signal, Figure 3.5 shows the input and output signals of a PFD when the input signal differs in frequency from the VCO signal by + 2 Hz. The reference signal was set to 3 Hz, and the input signal was 5 Hz. The PFD outputs logic high (+1) when both signals cross zero from negative to positive. If the VCO signal was greater in frequency than the input signal, the PFD would output negative logic high (-1). Due to the PFD output, the VCO decreases the frequency of the VCO signal and matches the input frequency after 0.4 seconds. Notice that the PFD output is a pulse train with the same frequency as the input signal.

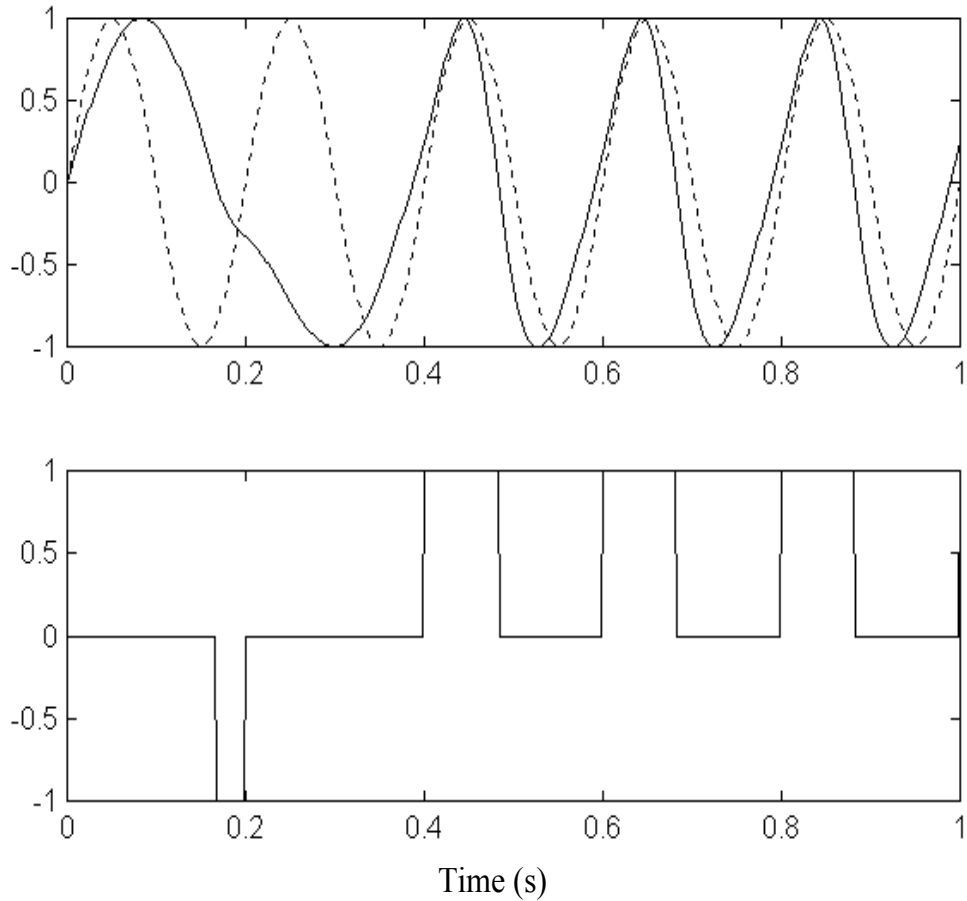


Figure 3.5: Top figure: VCO signal, solid line; Input signal, dashed line. Bottom figure: PFD output.

3.4 Behavior of the PLL in the Presence of Noise

3.4.1 Random Signals

Most of the benefits in using PLLs are due to the fact that they perform well in the presence of random noise, even if the signal-to-noise ratio is close to one. Random noise has the effect of both delaying and advancing the zero crossings stochastically, which causes a phase jitter in the PLL but does not cause it to lose frequency lock. Figure 3.6 shows the digital PLL simulated in MATLAB with a 3 Hz signal buried in random noise, and Figure 3.7 shows the corresponding ‘cleaner’ output of the VCO.

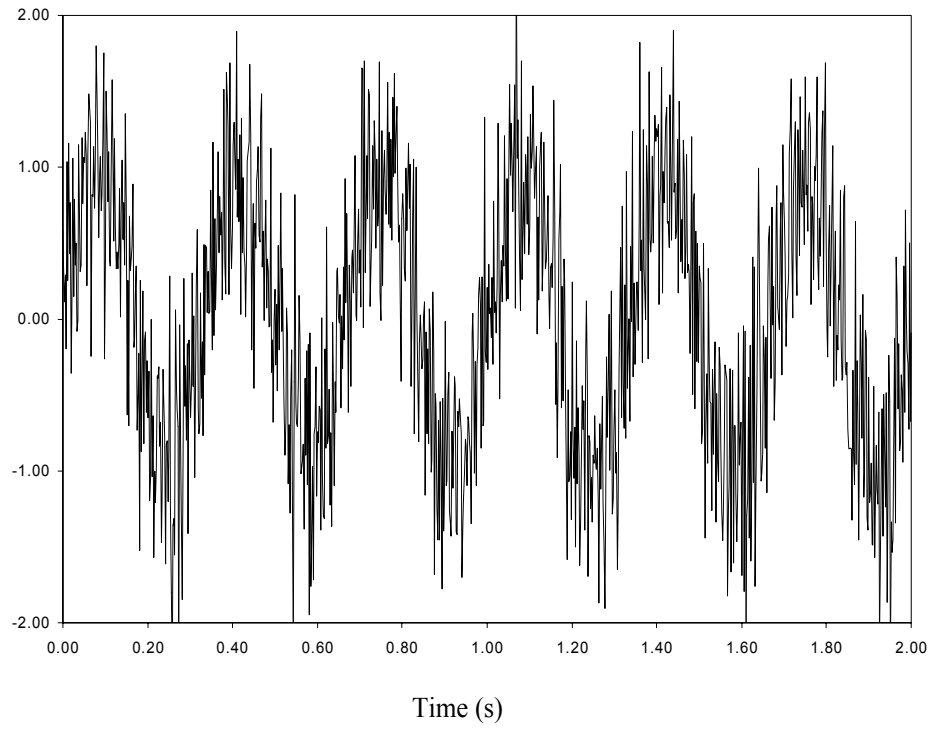


Figure 3.6: 3 Hz input signal to PLL with random noise.

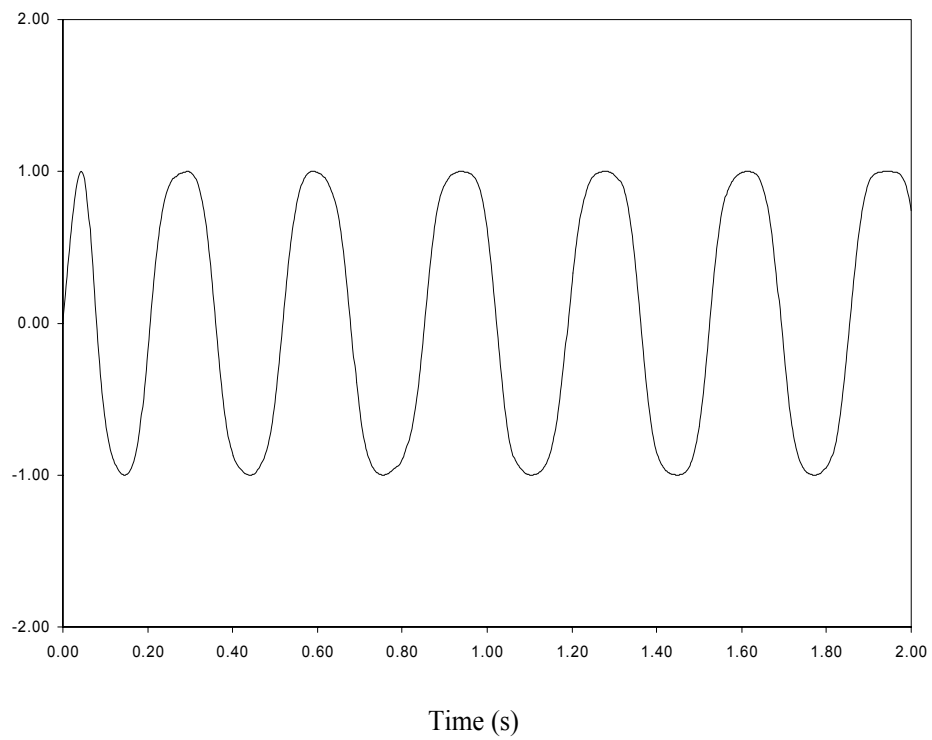


Figure 3.7: VCO output of PLL.

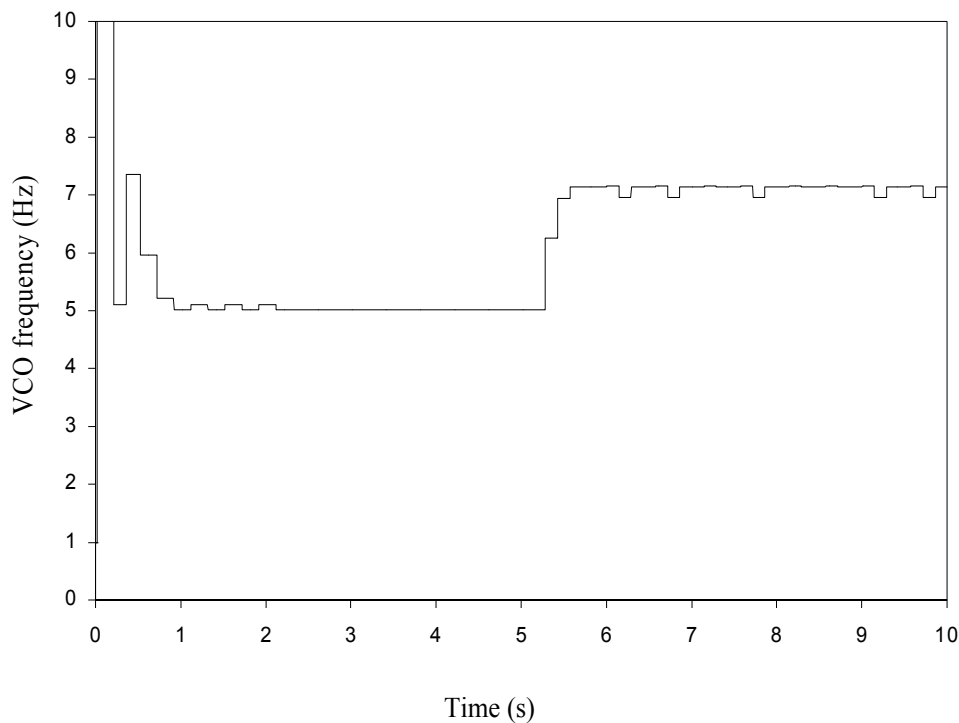


Figure 3.8: Simulated step response of digital PLL with a PFD.

3.4.2 Deterministic Signals

There is much analysis in the literature of the PLL behavior in the presence of random noise. However, there is little written on the behavior of a PLL when the ‘noise’ is not random but rather another deterministic signal present with the input signal. To characterize this behavior, further simulation with the digital PLL in MATLAB was necessary. The PLL algorithm was first simulated with a single sinusoidal signal.

With the initial VCO frequency set to 5 Hz, the input to the PLL was started at 5 Hz, then abruptly stepped to 7 Hz (see Figure 3.8). The PLL was found to quickly lock onto any signal within its capture range. To characterize the PLL performance in the presence of signals with multiple frequencies, the PLL was next simulated with signals of varying content. The input to the PLL for the second simulation was a sinusoidal signal comprised of two frequencies: one held fixed at 2 Hz, and another that was varied from 0 to 20 Hz. The PLL was given a reference frequency of 3 Hz, and the goal was to lock onto the 2 Hz frequency. The amplitude of the 2 Hz

signal was held constant at 1, and the ‘noise’ signal amplitude was increased until the PLL became unlocked from the 2 Hz signal. Figure 3.9 shows the results of this simulation. The signal-to-noise ratio (SNR) was smallest when the noise frequency was an integer multiple of 2 Hz, because the relative phase between the two signals was constant. The simulation also showed a lower SNR was necessary for lock at higher noise signal frequencies. This can be attributed to the fact that at high frequencies the noise signal is effectively out of the capture range of the PLL. However, the PLL still needs a SNR of at least 6.7 to lock onto the input signal. To determine if the PFD was contributing this poor performance, the same test was performed with a simpler analog-type PLL. As can be seen in Figure 3.10, the SNR necessary for lock at high noise signal frequencies is still about 4. These findings are consistent with the standard PLL design practice of using PLLs only when the signal-to-noise ratio is ≥ 4 [Best (1984)], and with the findings of Lu (1999). Structures that have higher frequency modes with amplitudes greater than or equal to the amplitude of the targeted mode could complicate the PLL behavior and keep it from tracking one particular mode. To observe this situation, another simulation was performed with the digital PLL. Figure 3.11 shows the simulation setup. A transfer function representing a structure with three lightly damped modes at 5, 10 and 20 Hz was excited by 500 Hz bandwidth random noise. The resulting noiseless output was differentiated to simulate a rate sensor and to amplify the higher frequency modes. This was motivated by the fact that pointing control tests performed on the MACE-II test article use angular rate gyros as sensors. This rate signal was then input to a PLL with an initial VCO frequency of 5 Hz. Figure 3.13 shows the time history and power spectral density estimate of the PLL input signal. Looking at the resulting PLL output signal frequency in Figure 3.12, it is clear that the PLL deviates many times a second from the 5 Hz signal. If the PLL was setting the frequency of a PPF filter based on this measurement, it would be suboptimal and possibly destabilizing.

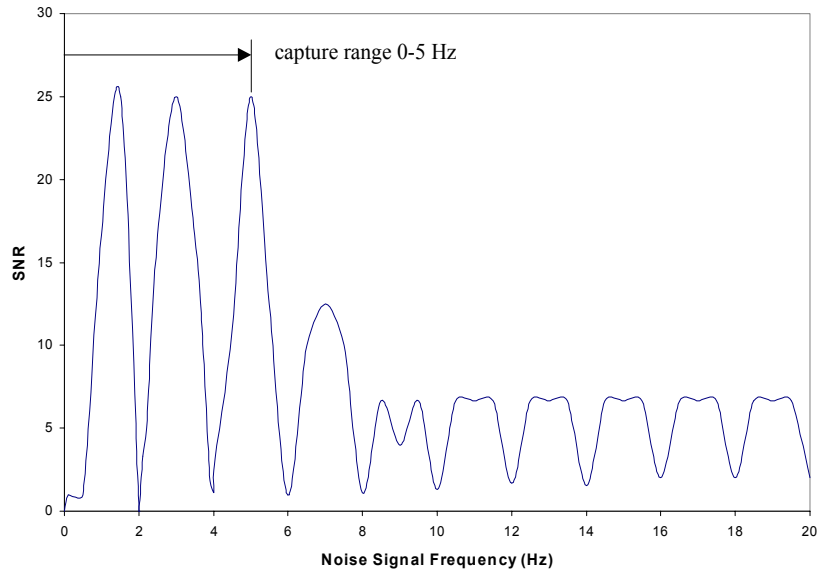


Figure 3.9: Signal-to-noise ratio required for lock versus noise frequency, digital PLL with Type-II PFD.

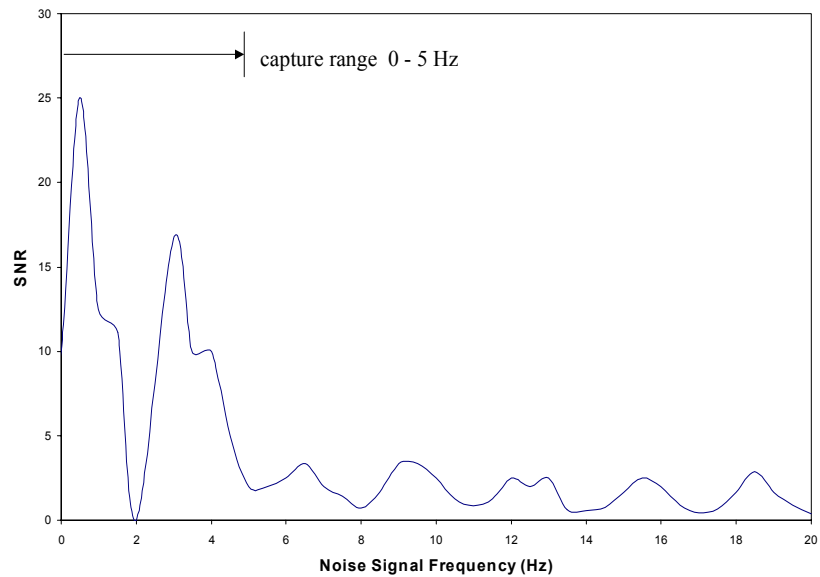


Figure 3.10: Signal-to-noise ratio required for lock versus noise frequency, analog PLL.

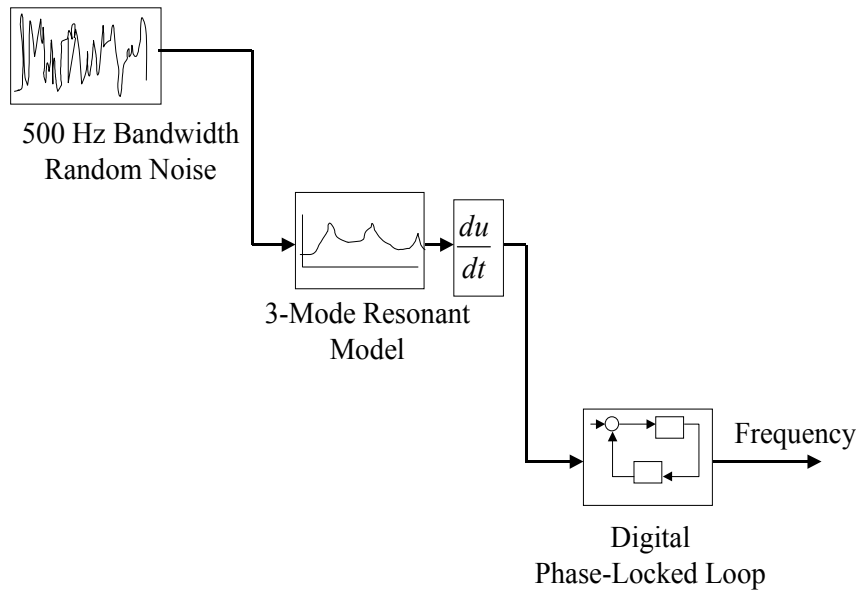


Figure 3.11: Simulation of digital PLL tracking ability with broadband excitation.

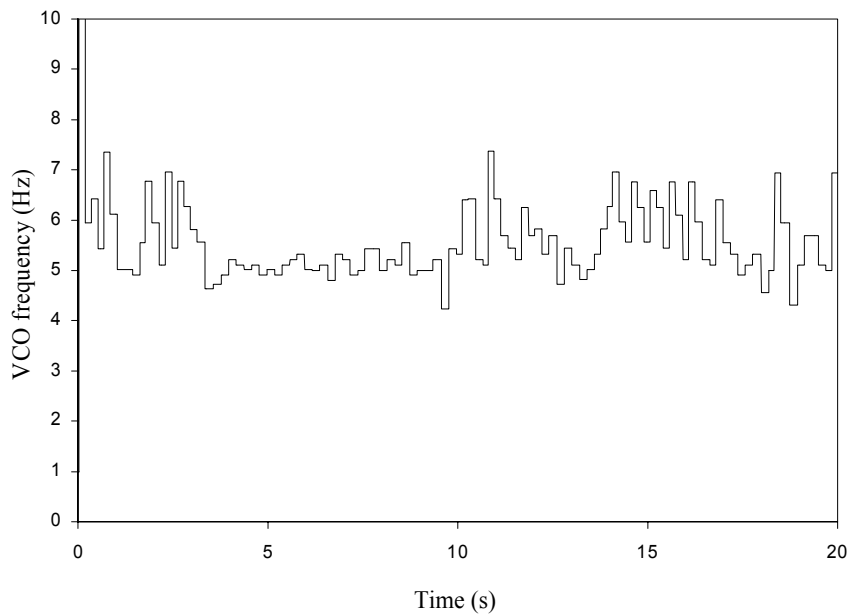


Figure 3.12: PLL output frequency from excitation of resonant system with 500 Hz noise.

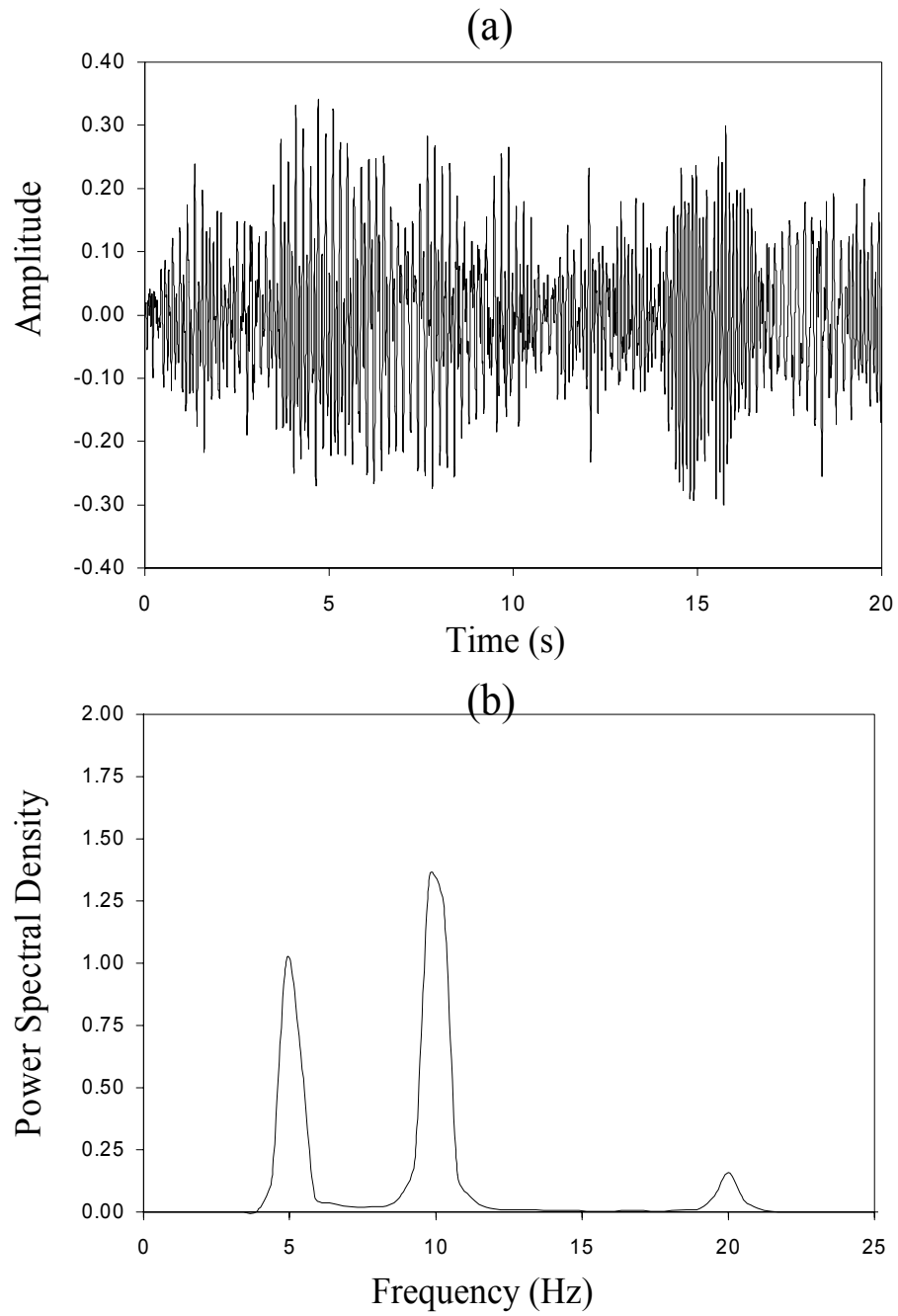


Figure 3.13: (a) Time history of PLL input signal; (b) Power spectral density estimate of PLL input signal.

3.5 Summary

Different types of PLLs were analyzed and the process by which a PLL obtains lock was studied. The output of the phase-frequency detector as a function of its two input signals was discussed. The behavior of analog and digital PLLs in the presence of random and deterministic signals was simulated. The simulations yielded the following conclusions:

1. PLLs need a signal-to-noise ratio of at least 4 to obtain lock, when the noise signal is actually another sinusoidal signal at a higher frequency.
2. If a PLL uses a rate signal from a structure vibrating in multiple modes to tune a PPF filter, deviations in the PLL output could be destabilizing.
3. A PLL using a rate-type signal as its input would need to include a bandpass filter to eliminate the frequency content outside the bandwidth of interest.
4. PLLs are useful for structural control if the disturbance is tonal or narrowband.

Chapter 4

Experimental Results

The on-line PPF design algorithm and phase-locked loop were tested on a variety of structures. Some of the experimental results in this work were obtained on the Middeck Active Control Experiment II (MACE-II) test article at Kirtland Air Force Base in Albuquerque, NM. The other experiments were performed on two structures at Virginia Tech, a test rig similar to the MACE test article and a simply-supported plate.

4.1 Simply-Supported Plate

4.1.1 Test Setup

The simply-supported plate shown in Figure 4.1 was constructed of 1/8" x 8" x 12" 6061 aluminum. The control actuator was a collocated pair of Piezo Systems .010" x 1" x 1 1/2" PZT-5A PZT piezoceramic patches attached on either side. The output was provided by a Kistler accelerometer model 8628 B50 with a sensitivity of 100 mV/g. The closed-loop results were obtained by exciting the plate with a modal hammer 1" from the top right corner (see Figure 4.1). This location adequately excited both the first and second modes. The experimental setup is shown in Figure 4.2. Realtime control was provided by a dSPACE DS1102 controller board with a TMS320C31 floating-point digital signal processor. The control algorithm was

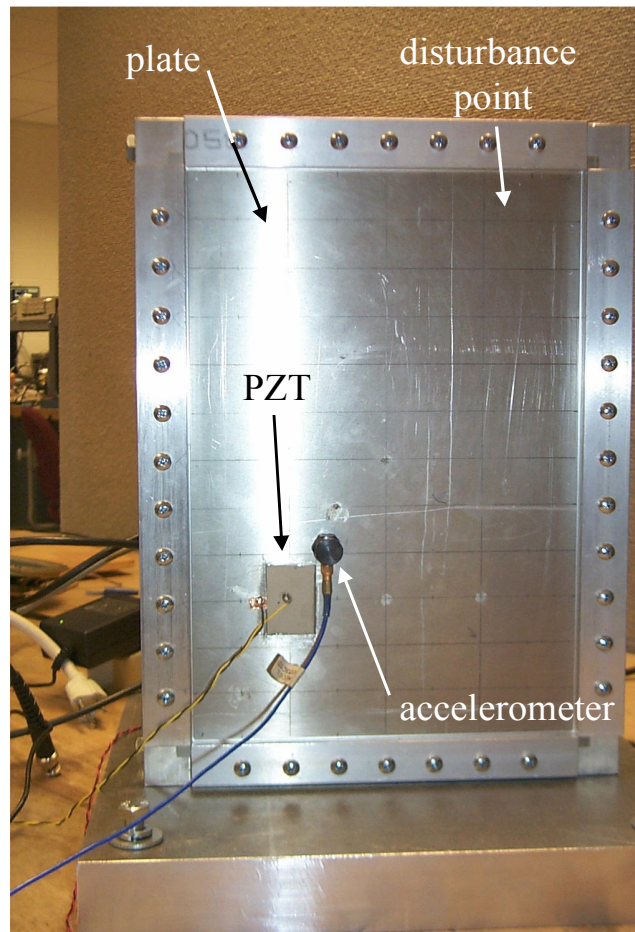


Figure 4.1: Simply-supported plate experiment.

designed in a SIMULINK block diagram, and the Realtime Workshop was used to generate C code and download to the DS1102 board. The acceleration signal was integrated twice in the realtime code to provide the position measurement for the PPF filters. The two integrators had a zero at zero frequency to eliminate any DC offset in the accelerometer signal. The PPF filters and integrators were discretized using the Tustin transformation $s = \frac{2}{T} \frac{z-1}{z+1}$. To decrease the effects of the phase lag added by the discretization, the control was run at a sample rate of 15 kHz. However, the pole/zero identification algorithm was much more computationally intensive and could not be performed within 1/15000 of a second. Therefore, the pole/zero identification running at 5 kHz was performed first, and the closed-loop control portion of the algorithm was run separately at 15 kHz with the PPF filters designed by the identification routine.

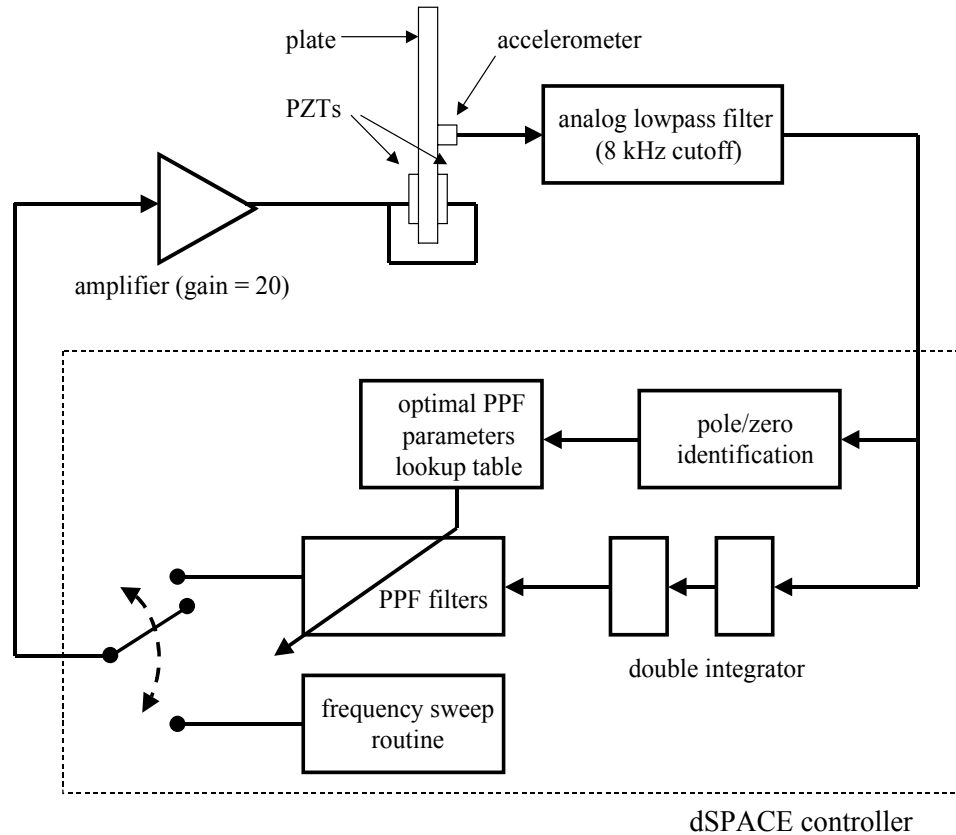


Figure 4.2: Test setup and control architecture for plate experiment.

4.1.2 Results

Figure 4.3 shows the experimental frequency response of the control-to-output transfer function. Even though the PZTs and accelerometer were not spatially collocated, the frequency response is adequate for the optimal PPF design because it exhibits the necessary pole/zero interlacing up to the second mode. The pole/zero identification routine was performed twice, once with a frequency sweep of 200-400 Hz to design the first mode PPF filter, and the other from 400-700 Hz to design the second mode PPF filter. Table 4.1 illustrates the accuracy of the pole/zero identification routine. The ‘actual’ frequency was measured from experimental frequency response data taken with a Tektronix Fourier Analyzer.

Figure 4.4 shows the closed-loop performance using the first mode PPF filter. The filter successfully increased the damping in the first mode by a factor of 6 from

Table 4.1: Results of experimental pole/zero identification on simply-supported plate.

Pole/Zero	Identified Frequency (Hz)	Actual Frequency (Hz)	Error (%)
1st pole	258	257	+0.4
1st zero	327	318	+2.8
2nd pole	493	490	+0.6
2nd zero	628	615	+2.1

0.8% critical to 5% critical, resulting in a 20 dB reduction in magnitude. The DC gain margin was estimated from experimental frequency response data of the loop transfer function containing the PPF filter and found to be approximately 2. Using equation (2.36) in Chapter 2 with this gain margin and pole/zero ratio, the theoretical closed-loop damping was expected to be 14% critical. The simulated closed-loop frequency response was calculated by substituting the experimental loop transfer function data $G_{LOOP}(j\omega)$ and experimental open-loop disturbance-to-output data $G_{yd}(j\omega)$ into the following equation:

$$|G_{yd}(j\omega)|_{CL} = \left| \frac{G_{yd}(j\omega)}{1 - G_{LOOP}(j\omega)} \right| \quad (4.1)$$

Because it uses actual experimental open-loop data, the simulated closed-loop frequency response should approximate the experimental closed-loop frequency response. The difference indicates uncertainty in these closed-loop results. The sensitivity of the accelerometer was so high the plate had to be struck with the modal hammer extremely gently to avoid overloading the spectrum analyzer. If the closed-loop system was very magnitude sensitive, this could explain why the experimental results do not match the theoretical results. However, since the open-loop data was also taken with the modal hammer, the relative damping between the open-loop and closed-loop case is more certain.

Figure 4.5 shows the closed-loop results of the second mode PPF filter designed with the pole/zero algorithm. The amount of damping was increased by a factor of 30 from 0.1% critical to 3% critical. The amount of damping in the first mode was also

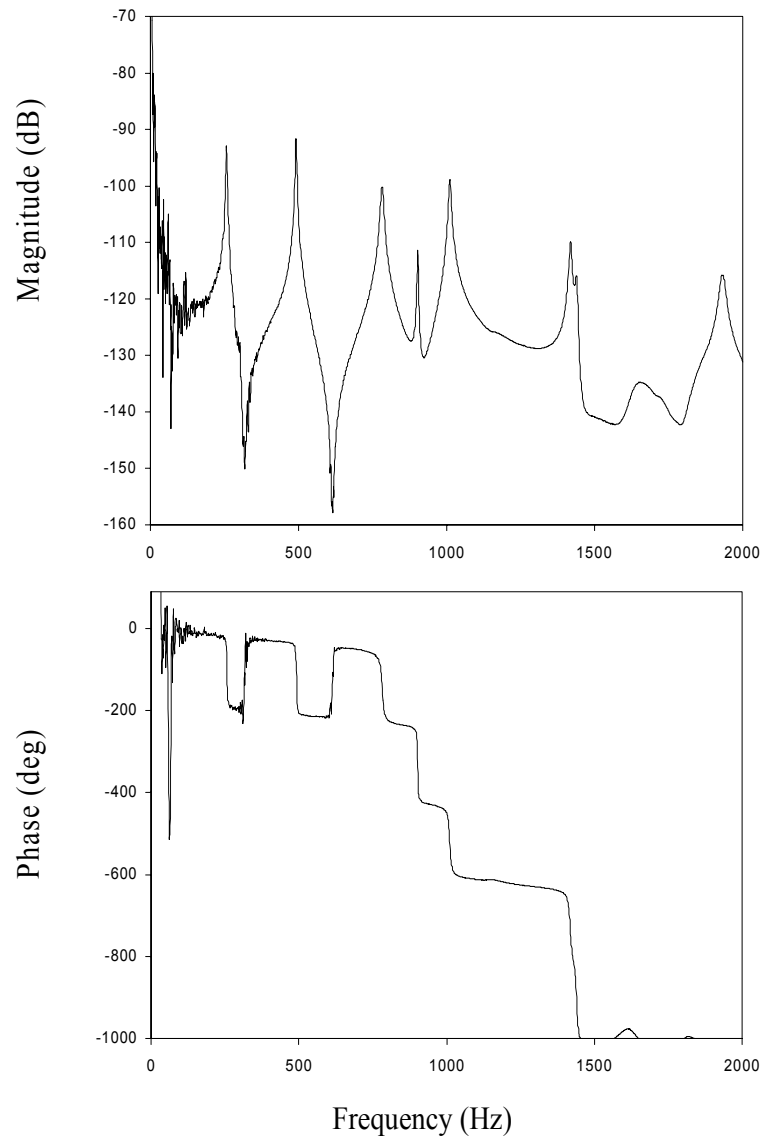


Figure 4.3: Frequency response of plate control-to-output transfer function.

increased by a factor of 2.3, suggesting that the modes are sufficiently close enough to be controlled by one filter. For this test, the PPF filter gain had to be limited due to a phase crossover in the region of the third mode. This can be attributed to the phase lag associated with the sample period delay, which is not an issue in the theoretical model because the phase is bounded between 0° and -180° . The phase lag also contributed to the decrease in damping performance as evident in the difference between the simulated and experimental results. The theoretical closed-loop damping calculated from the gain margin and pole/zero ratio was 17% critical, confirming the simulated results.

Figure 4.6 shows the closed-loop results with the two PPF filters connected in parallel to add damping to both modes. Each PPF filter gain was divided by two in order to keep the DC loop gain constant. The closed-loop result with both PPF filters was identical to the result with the second mode PPF filter, which did not yield as much damping in the first mode as the first mode PPF filter. Analysis of the PPF filters in parallel revealed that the phase lag at the frequency of the first mode was 17° more than with the first mode PPF filter alone. This phase difference was enough to cause the filter to be slightly suboptimal.

In all the experiments, the accelerometer signal had to be filtered with an analog lowpass filter. For the closed-loop PPF control experiments, the filter cutoff frequency was set to 8 kHz. This was necessary to eliminate aliased frequencies caused by exciting structural resonances above the Nyquist frequency. Also, the pole/zero identification routine generated an aliased frequency above the upper frequency bound of the frequency sweep which excited resonances outside the sweep bandwidth. This caused the identification routine to falsely identify poles at lower frequencies and to miss zeros in the frequency response. For the identification runs, the lowpass filter cutoff frequency was set to 800 Hz to eliminate the false resonances.

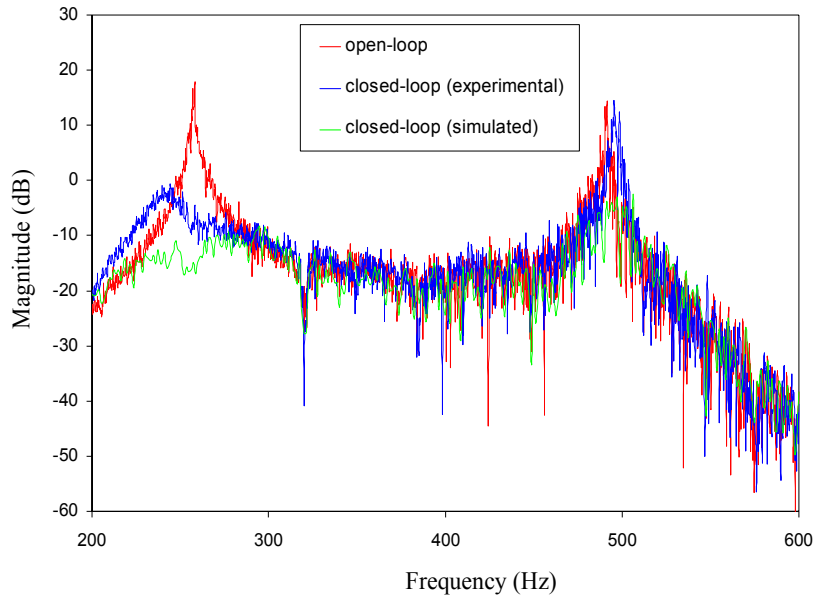


Figure 4.4: Frequency response of plate disturbance-to-output transfer function, 1st Mode PPF filter.

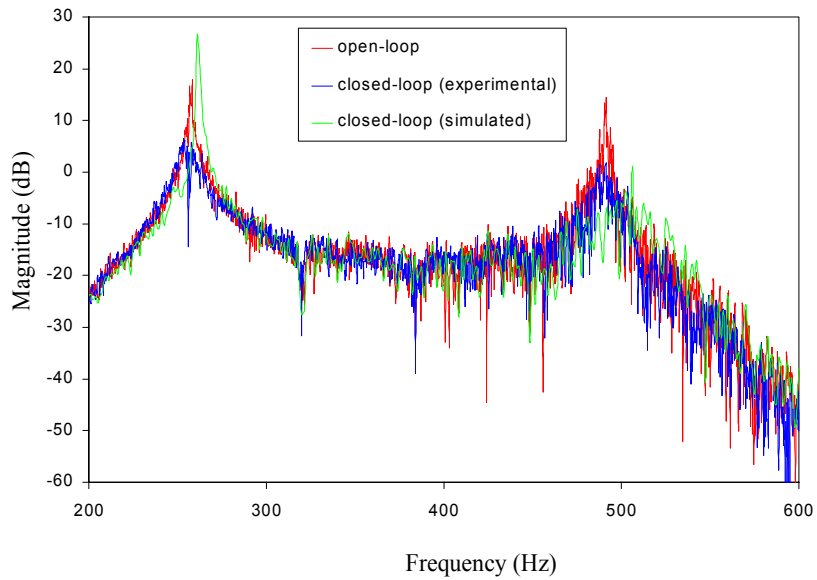


Figure 4.5: Frequency response of plate disturbance-to-output transfer function, 2nd Mode PPF filter.

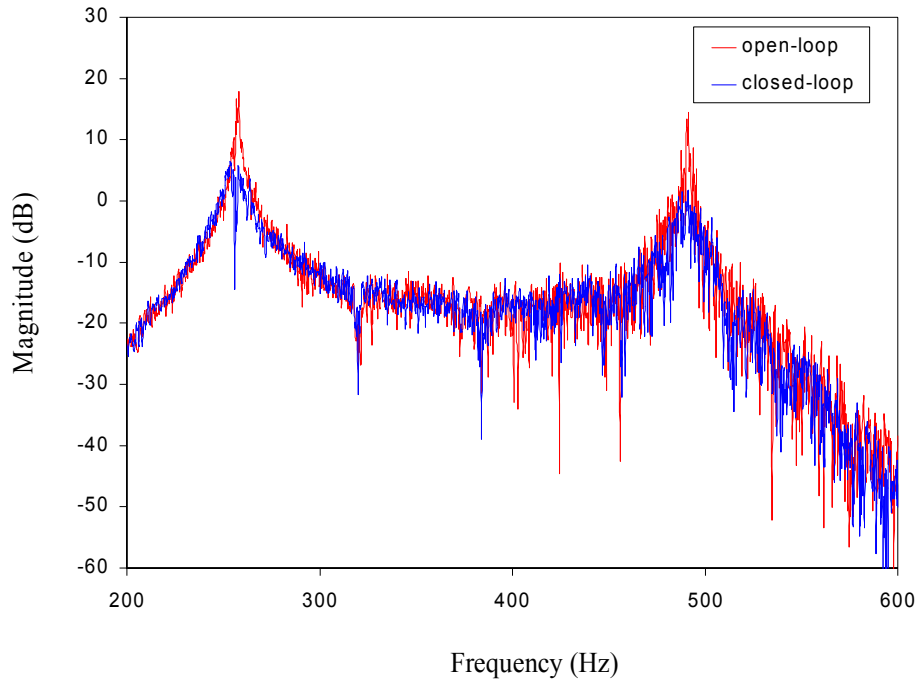


Figure 4.6: Frequency response of plate disturbance-to-output transfer function, both PPF filters in parallel.

4.2 MACE-II Experiment

Experiments involving the optimal PPF control and a phase-locked loop were performed on the MACE-II test article in Albuquerque, New Mexico. The results of these experiments will be used to design adaptive control algorithms for the MACE-II reflight in July 2000.

4.2.1 Test Setup

The MACE-II test structure has a pair of two-axis gimbal payloads connected by a bus composed of flexible struts. Reaction wheels at the center of the bus provide inertial attitude control. The entire test article is suspended by gravity offload cables to decouple the suspension dynamics from the structural dynamics. The structure has fifteen flexible modes below 60 Hz. Figure 1.1 in the Introduction shows a picture of the test article in configuration 1. All experimental results in this work were obtained

with the test article in this configuration.

Real-time control for the MACE test article is provided by a digital signal processor sampling at 500 Hz. There are nine actuators and twenty sensors available for the control algorithm. Since the control objective was to excite the secondary gimbal and maintain inertial pointing of the primary payload, the control actuator used for this work was the z-axis primary gimbal motor. The strain gauge adjacent to the primary end of the structure was used as the output sensor for the feedback control algorithm. The performance of the control algorithm was measured with the primary payload z-axis rate gyroscope. Figure 4.7 shows the primary gimbal with the actuators and sensors used with the control algorithm.

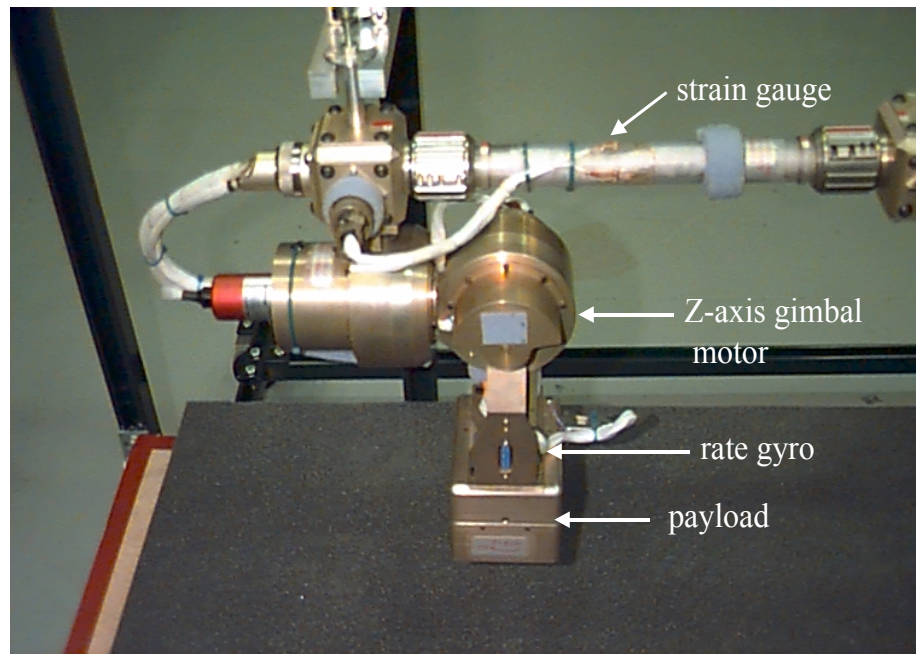


Figure 4.7: MACE-II primary gimbal.

4.2.2 Results - Phase-Locked Loop

The digital phase-locked loop algorithm was implemented in the MACE-II control software and tested with a variety of inputs. To make sure the PLL code compiled

correctly and could work on the MACE-II hardware, a simple test was performed by exciting the structure with a single tone and checking the PLL output. Once this was accomplished, the PLL behavior in a broadband noise environment was tested. The objective of the test was to determine if the PLL could maintain lock onto the 2 Hz bending mode while the structure was being excited by broadband noise. Using the same disturbance actuator and sensor as the first test, the PLL VCO was first initialized at the exact modal frequency of 2 Hz. Figure 4.8 shows the PLL VCO frequency during the broadband excitation. As expected, the PLL could not settle on 2 Hz because of the frequency content present in the signal (see power spectral density estimate in Figure 4.9). From the PLL simulations in Chapter 3, it is clear that the signal-to-noise ratio of the 2 Hz mode to the other modes is not high enough for the PLL to obtain lock.

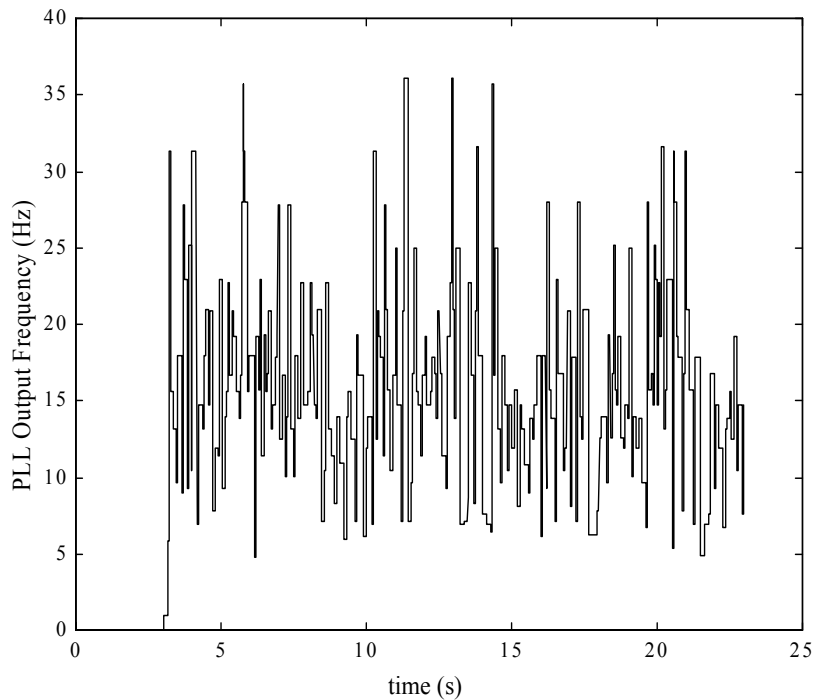


Figure 4.8: PLL output frequency with 100 Hz bandwidth noise disturbance (PLL algorithm initialized at $t = 3$ sec).

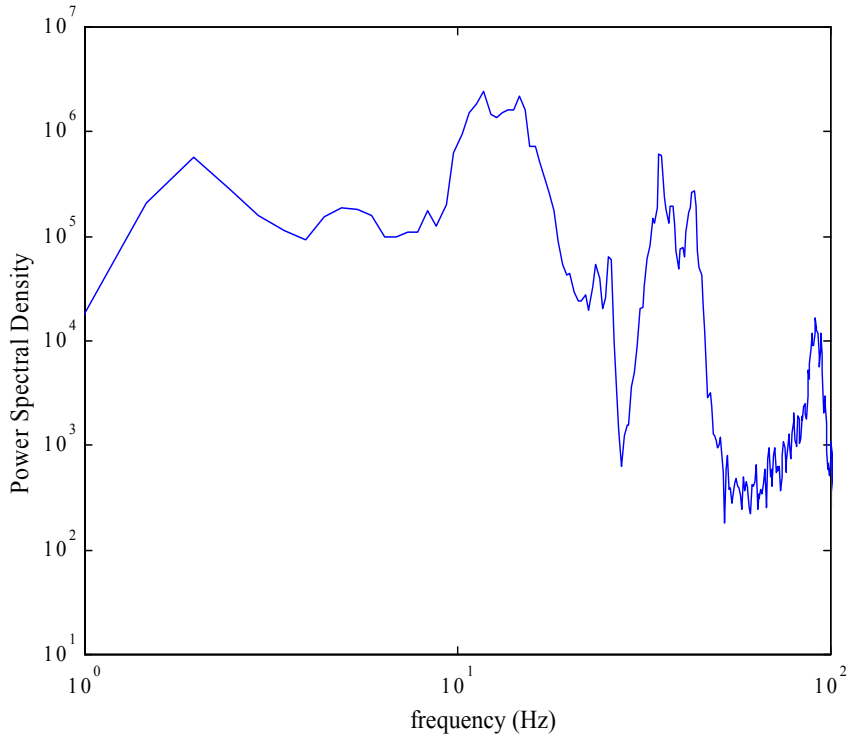


Figure 4.9: Power spectral density estimate of sensor signal from broadband noise PLL test.

4.2.3 Results - Optimal PPF Design

The optimal pole/zero PPF design algorithm was tested on the MACE-II test article. In order to only test the performance of the design algorithm, the pole/zero identification routine was not tested. The pole/zero ratio was determined off-line from frequency response data. The output sensor used for this algorithm was the strain gauge adjacent to the primary end, and the control actuator was the primary gimbal motor (see Figure 4.7). The goal of the MACE-II experiment is to minimize the response of the payload due to a structural disturbance, and the performance metric is the minimization of the payload angle measured by integrating the payload angular rate gyroscope. The disturbance source was the secondary gimbal motor. The open-loop experimental frequency response data was taken and placed in the form of this transfer function matrix:

$$G(j\omega) = \begin{bmatrix} G_{zd}(j\omega) & G_{zc}(j\omega) \\ G_{yd}(j\omega) & G_{yc}(j\omega) \end{bmatrix} \quad (4.2)$$

where z is the performance output, y is the sensor output, d is the disturbance input, and c is the control input. Figure 4.10 shows the block diagram of the closed-loop system including the performance and sensor output variables.

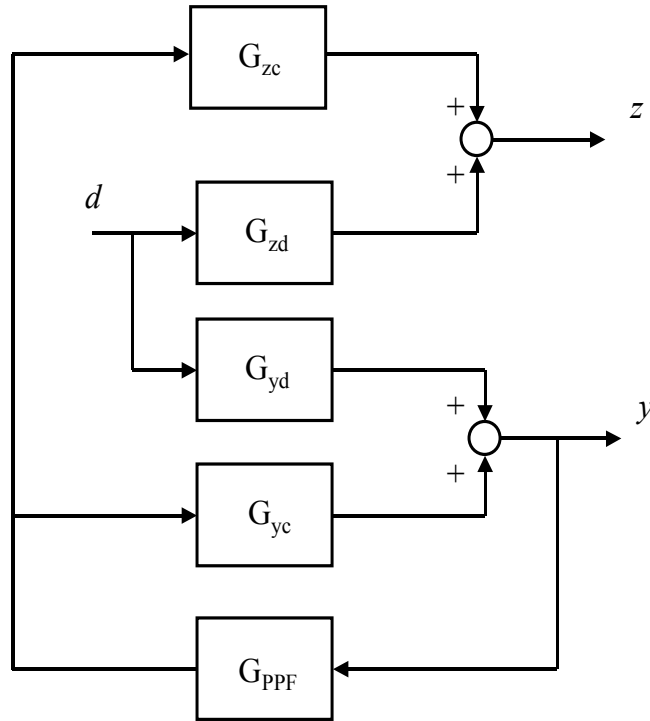


Figure 4.10: Block diagram of closed-loop system including performance variable.

Looking at Figure 4.10 the magnitude of the closed-loop disturbance-to-performance frequency response can be written:

$$|G_{zd}|_{CL} = \left| \frac{G_{zd} - G_{zd}G_{yc}G_{PPF} + G_{zc}G_{yd}G_{PPF}}{1 - G_{yc}G_{PPF}} \right|_{s=j\omega} \quad (4.3)$$

and the magnitude of the closed-loop disturbance-to-output frequency response can be written:

$$|G_{yd}|_{CL} = \left| \frac{G_{yd}}{1 - G_{yc}G_{PPF}} \right|_{s=j\omega} \quad (4.4)$$

With the simulated frequency response of the PPF filter, the simulated closed-loop frequency response can be obtained by solving equations (4.3) and (4.4). To add damping to the first bending mode at 2 Hz, a PPF filter was designed with the optimal parameters using the pole/zero ratio from the experimental G_{yc} frequency response data, shown in Figure 4.11. Because of the noncollocation of the strain gauge and gimbal motor, the transfer function does not appear to exhibit the typical collocated pole/zero interlacing. However, there is a zero that occurs at 9 Hz after the 2 Hz first bending mode, as evident in the phase jump from 0° to 50° . This allows the optimal PPF filter to be designed based on the 9 Hz / 2 Hz ratio.

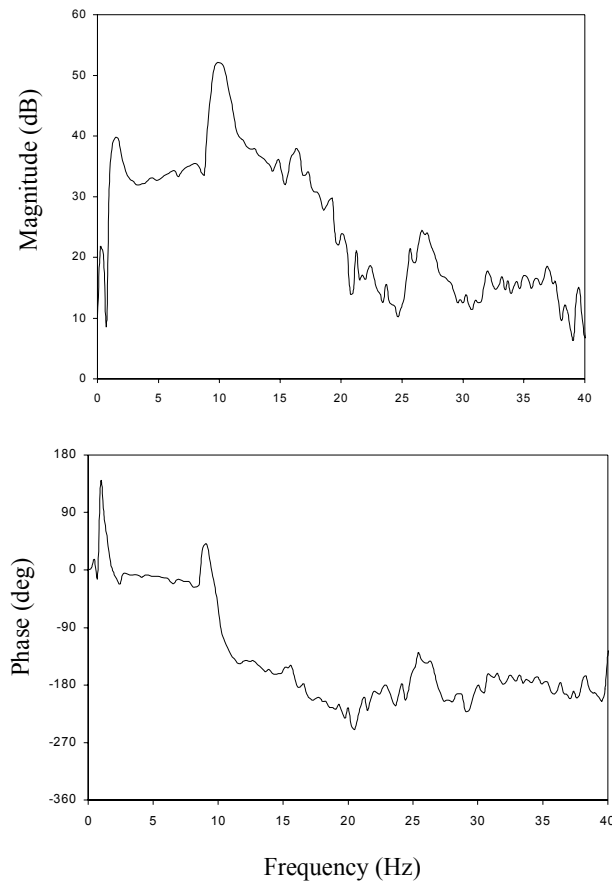


Figure 4.11: Experimental control-to-output transfer function.

The PPF frequency response was used in equations (4.3) and (4.4) to find the simulated closed-loop frequency response. The closed-loop experimental results are plotted versus the open-loop experimental data and the simulated closed-loop data in Figures 4.12 and 4.13 for the disturbance-to-output and disturbance-to-performance respectively. The optimally designed PPF filter performed well, reducing the magnitude of the disturbance-to-output by 18 dB at the first mode. However, this was accomplished by actuation of the payload in the fashion of a tuned vibration absorber, as evident from the increased motion of the payload in Figure 4.13. As will be discussed in the summary, the type of low-authority PPF controller implemented in this algorithm is better suited to adding structural damping rather than precise pointing control.

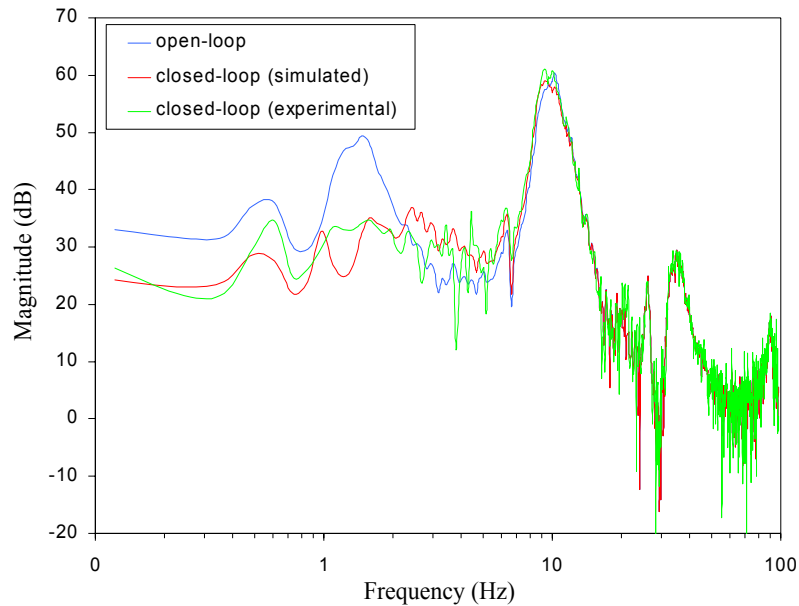


Figure 4.12: Frequency response of disturbance-to-output using PPF controller designed with pole/zero algorithm.

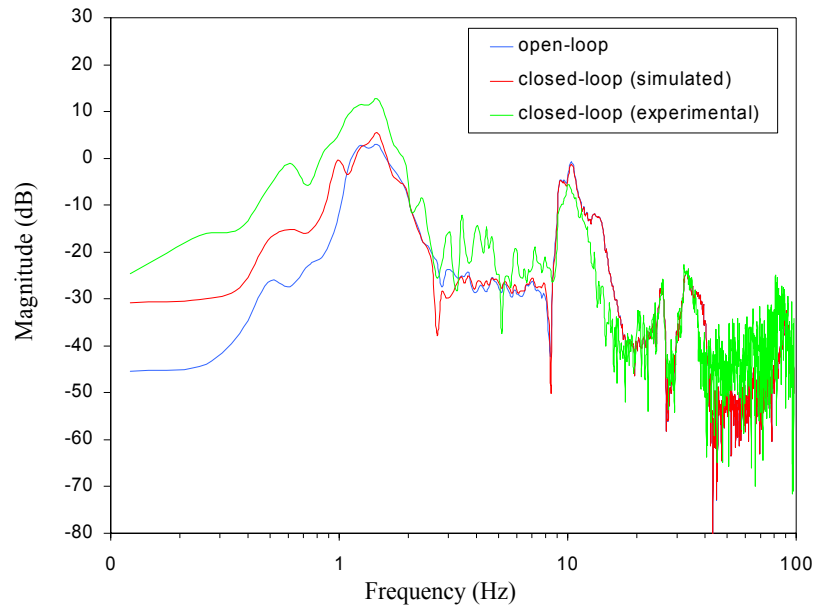


Figure 4.13: Frequency response of disturbance-to-performance using PPF controller designed with pole/zero algorithm.

4.3 Mini-MACE

In order to test MACE-II control algorithms at Virginia Tech, a test stand was designed and fabricated. Named the Mini-MACE, it was designed to have similar structural dynamics, actuators, and sensors as the MACE test article. Figure 4.14 shows a picture of the Mini-MACE test structure.

4.3.1 Test Setup

The Mini-MACE was constructed of two lengths of steel rod connected by a node and fixed at one end to form a cantilevered structure. To provide the disturbance source, an electromechanical shaker was mounted at the middle node. To simulate the gimbal payload on the MACE, a DC motor was attached to the end node. A payload mass was then attached to the motor shaft, and accelerometers were used to measure the output and performance variables. The entire structure was designed to have a first bending mode around 3 Hz. The DC motor was a Clifton Precision permanent magnet servo motor model number JDH-2250-BK-DC. The accelerometer used for the

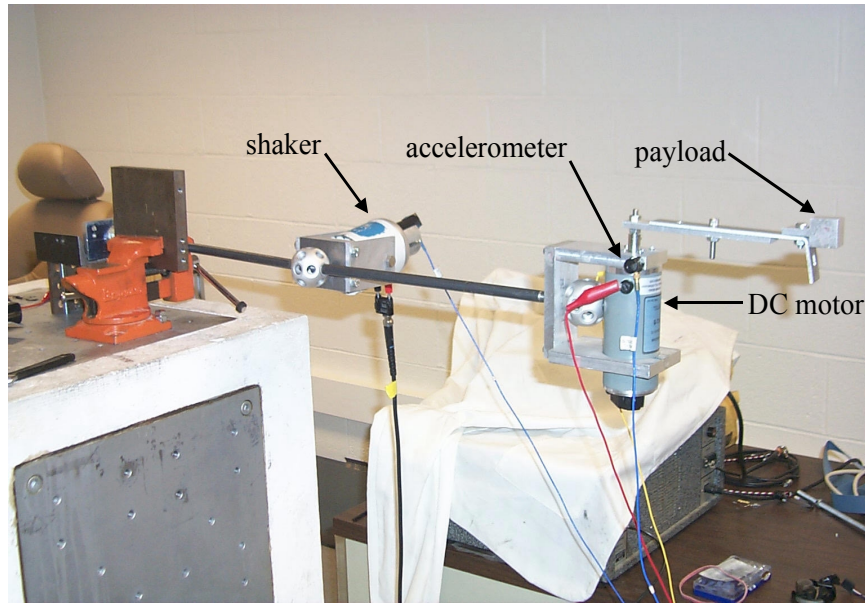


Figure 4.14: Mini-Mace test structure.

output sensor was a PCB model 3206 C38 with a sensitivity of 100 mV/g, and the payload accelerometer was a Kistler model 8628 B50 with a sensitivity of 100 mV/g. The control hardware was identical to the simply-supported plate experiment. The control algorithm was implemented in SIMULINK, coded by the RealTime Workshop and downlinked to the dSPACE controller board. The sample rate was set at 500 Hz, the same as the MACE hardware. This longer sample period allowed the complete on-line algorithm to be tested in one seamless routine. As seen in Figure 4.14, the output accelerometer was placed at the end of the bus next to the motor mount, and the performance accelerometer was placed on the payload.

4.3.2 Results

Due to a high amount of stiction in the DC motor, there was significant deadband in the closed-loop system. A high level of structural excitation was needed for the motor shaft to overcome this stiction. The shaker was not large enough to provide this level of excitation, so the closed-loop damping added by the feedback control was estimated from transient responses.

The pole/zero algorithm was performed in the bandwidth of the first mode, and an optimal PPF filter was designed on-line from the lookup table. Figure 4.15 shows the open-loop and closed-loop transient responses. The optimal PPF filter increased the damping in the structure from 1% critical to 9% critical. Figure 4.16 shows the payload acceleration during the same transient tests. As in the MACE-II experiments, the payload motion was increased due to the slewing action of the motor. The following section analyzes the causes of this behavior in relation to the optimal PPF control algorithm.

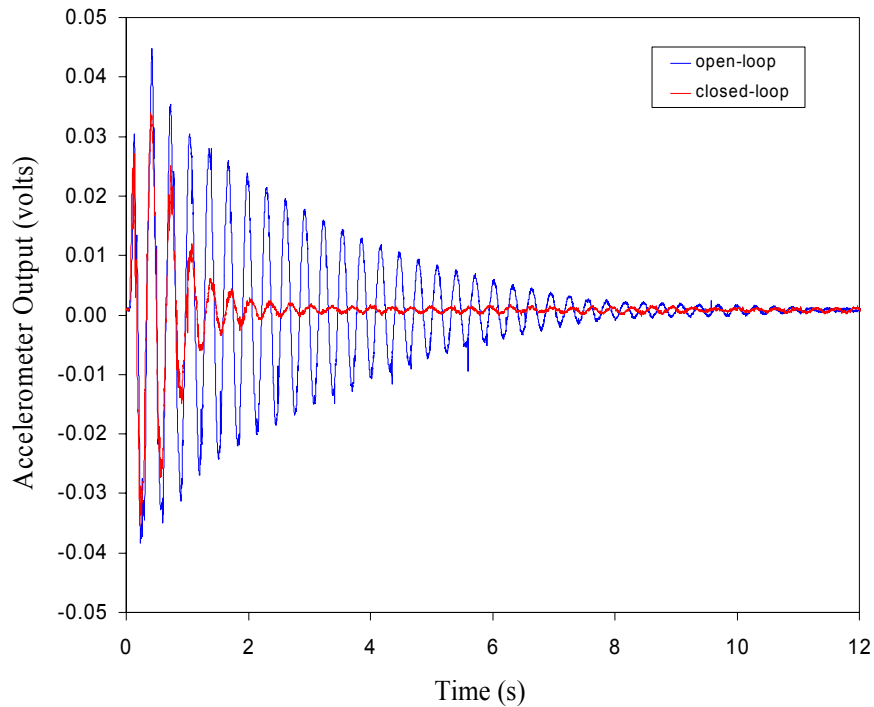


Figure 4.15: Closed-loop transient bus acceleration using PPF controller designed with pole/zero algorithm.

4.4 Analysis of Payload Response

It is clear from the experimental results that the PPF controller designed with the optimal algorithm was successful at adding structural damping in all three test articles. However, for the Mini-MACE and MACE-II tests, the control objective was

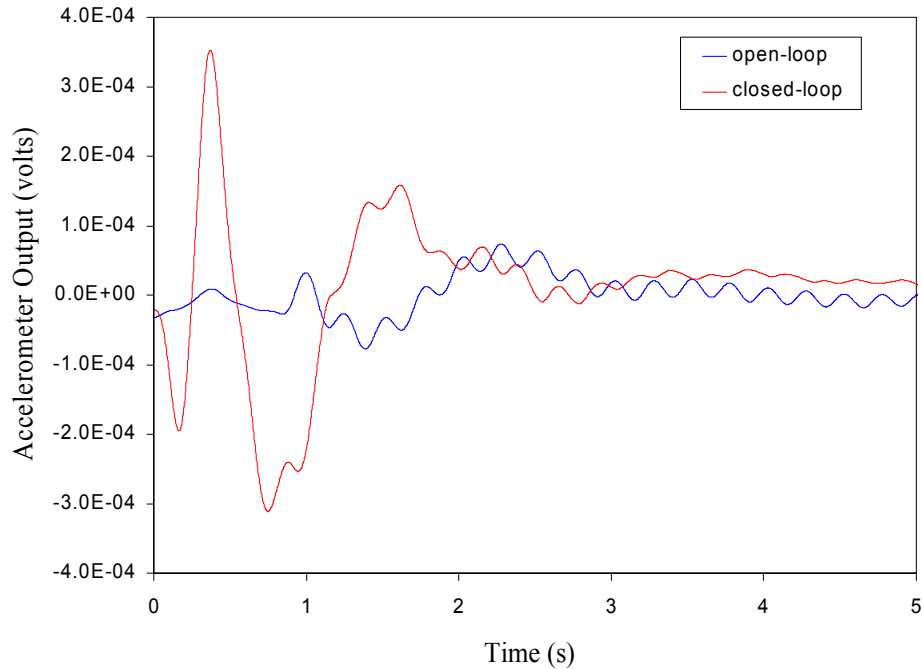


Figure 4.16: Closed-loop transient payload acceleration using PPF controller designed with pole/zero algorithm.

to minimize the motion of a payload attached to a control motor in the presence of a disturbance. In both closed-loop experiments, the payload response was increased from the open-loop case, indicating that the motor was slewing the payload back and forth to control the structure. This phenomenon can be explained by looking at the numerator of equation (4.3). The magnitude of the numerator does not necessarily decrease if the PPF filter changes the magnitude and phase of the loop transfer function $G_{yc}G_{PPF}$. Depending on the magnitude and phase of the disturbance-to-performance and disturbance-to-output paths, the overall performance magnitude could be increased by closing the loop. Another way of describing the vibration absorber phenomenon is to analyze a simple model of a spring-mass connected to a pinned rod with length L as shown in Figure 4.17. The rod is free to swing and there is no damping or gravity in the system. A control torque T_C is applied to the rod to decrease the response of the mass position due to the disturbance force F_D . The equations of motion for the uncontrolled system are [James et al. (1989)]:

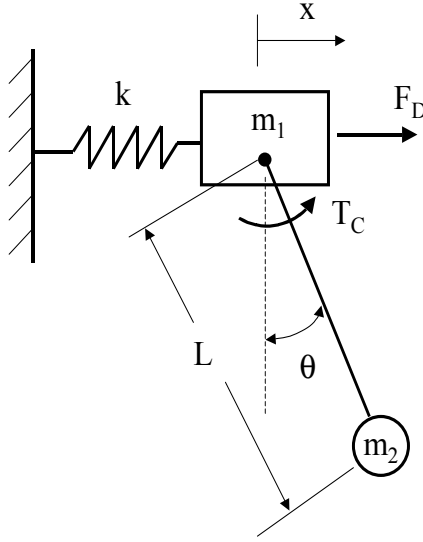


Figure 4.17: Spring-mass with pinned rod and mass.

$$\begin{bmatrix} (m_1 + m_2) & m_2L \\ m_2L & m_2L^2 \end{bmatrix} \begin{Bmatrix} \ddot{x} \\ \ddot{\theta} \end{Bmatrix} + \begin{bmatrix} 2k & 0 \\ 0 & 0 \end{bmatrix} \begin{Bmatrix} x \\ \theta \end{Bmatrix} = \begin{Bmatrix} F_D \\ T_C \end{Bmatrix} \quad (4.5)$$

Looking at equation (4.5), the uncontrolled rod angle θ has a rigid body mode associated with the zeros in the stiffness matrix. If the position x of the mass m_1 is used as the feedback variable for a simple proportional control law $T_C = -K_p x$, then the closed-loop stiffness matrix becomes

$$\begin{bmatrix} 2k & 0 \\ K_p & 0 \end{bmatrix} \quad (4.6)$$

and is now coupled due to the off-diagonal term. The rod angle now has a mode associated with the position of m_1 . Since we are modeling this system after the Mini-MACE and MACE-II test articles, it is appropriate to define the performance z as the absolute position of m_2 , or $z = x + L \sin \theta$. Even if x due to the disturbance force

is minimized, θ and therefore z could be increased due to the coupling introduced by the feedback control law.

Because the performance is to be minimized by the control, it would seem logical to use the performance variable in the feedback loop. However, the transmission path between the payload motor and payload angular rate is rigid and therefore does not have the pole/zero interlacing typical of a flexible structure. The entire optimal PPF design algorithm is based on the pole/zero spacings of a control-to-output transfer function that exhibits pole/zero interlacing typical of a collocated actuator/sensor pair. This was the motivation for using the structural motion as the feedback variable rather than the payload motion in the MACE-II and Mini-MACE experiments. Using the payload angular rate or acceleration as the feedback variable would make the optimal PPF algorithm inapplicable to the control problem.

4.5 Summary

The on-line optimal PPF design algorithm was tested on three different structures and shown to be very effective at adding structural damping to the first one or two modes. The pole/zero identification routine could accurately identify the pole and zero frequencies in a structure with low damping. The optimal PPF algorithm was shown to work well even if the actuator/sensor pair was not spatially collocated, as long as the control-to-output frequency response exhibited pole/zero interlacing in the bandwidth of interest. The optimal PPF controllers were ineffective at pointing control of the payloads on the Mini-MACE and MACE-II test articles and actually increased the payload motion from the open-loop case. A simple mass and pinned rod system was analyzed to explain this behavior, and the results were found to be caused by an improper choice of sensor. However, the proper sensor for pointing control of a MACE-II type test article would yield an undesirable control-to-output frequency response. Therefore, the on-line optimal PPF algorithm is ineffective at vibration isolation of rigid bodies. The phase-locked loop algorithm was also tested on the MACE-II hardware. The PLL could track a single disturbance tone applied

to the structure, but could not discern one structural mode from another when the structure was excited with broadband noise.

Chapter 5

Conclusions

Flexible structures are susceptible to unwanted vibrations particularly if they are constructed of materials with low damping. Structures such as satellites have design criteria which limit the amount of mass or stiffness that can be incorporated in the structure. An active control system is necessary to add damping to the resonant structural modes. For structures with time-varying dynamics, the control algorithm must be able to adaptively update itself in realtime to maintain performance. An optimal control algorithm based on identification of certain structural parameters on-line could be used adaptively.

A feedback control law based on Positive Position Feedback (PPF) filters was analyzed in a simple model. The control-to-output transfer function of the model exhibited pole/zero interlacing typical of a collocated actuator/sensor. The amount of closed-loop damping a PPF filter could add was shown to monotonically increase with the amount of frequency spacing of the pole/zero pair. At exact pole/zero cancelation, the controller cannot add any damping because the control authority has been diminished.

Optimal locations for the closed-loop poles of the controlled structure were defined as the point where the poles have equal damping ratios. The optimal closed-loop characteristic equation was then defined, as well as the characteristic equation formed from the PPF control law. Pole placement was performed with these two forms of the closed-loop characteristic equation. This yielded equations for the optimal PPF

damping ratio and frequency as functions of the pole/zero spacing in the control-to-output transfer function. By solving these equations, optimal PPF parameters for a range of pole/zero spacings were generated. These optimal PPF parameters could then be stored in a lookup table to be used for the on-line PPF design.

An on-line pole/zero identification routine was developed to design optimal PPF filters in realtime. The routine uses the control actuator to sweep through all frequencies between user-specified bounds. The resulting sensor signal is filtered and conditioned so a running maximum and running minimum loop can identify the frequencies at which the pole and zero occur. Once these frequencies are known, the pole/zero ratio is used to design the optimal PPF filters from the parameters in the lookup table.

A phase-locked loop (PLL) was analyzed and simulated in the presence of random and deterministic signals. The different types of phase detectors were also studied. Simulations showed the PLL accurately tracked changes in a single tone, even if the signal was heavily buried in random noise. However, they also showed that the PLL required a signal-to-noise ratio of at least four if the noise signals were deterministic signals at frequencies across the spectrum. If a PLL was being used to track a structural mode in a structure excited by broadband noise, the other modes could prevent the PLL from obtaining lock. Experimental results verified this conclusion. If a PLL is to be used in such a manner, the input signal would need to be filtered with a narrow bandpass filter to eliminate the frequency content of the other modes. This requirement would limit the usefulness of a PLL for the problem studied in this thesis.

The on-line optimal PPF algorithm was tested on three structures with different dynamics, actuators, and sensors. Results with a simply-supported plate showed that the algorithm was very effective at identifying the poles and zeros accurately to within 2.5% of the actual values. The optimal PPF filters were effective at adding damping to resonant modes in both the single and multiple PPF cases. For the single PPF cases, the optimal PPF filter increased the damping from 0.8% critical to 5% critical in the first mode, and from 0.1% critical to 3% critical in the second mode.

The expected values based on the theoretical model were 14% critical and 17% critical for the first and second modes, respectively. The simulated closed-loop response obtained from experimental frequency response data indicated that there may have been problems with the manner in which the plate was excited. The actuator and sensor of the simply-supported plate were PZTs and an accelerometer, respectively. Even though they were not collocated and not dual (angular moment - linear acceleration), the optimal algorithm could still design the optimal PPF filters. The only criteria for the optimal algorithm is that the control-to-output transfer function exhibit pole/zero interlacing in the bandwidth of interest.

The other two structures, the Mini-MACE and MACE-II test articles, had different control objectives than the plate experiment. Instead of simply adding damping to the structure, the goal of these experiments was to isolate a payload from a structural disturbance using a control motor. Because the control motor to payload sensor transfer function did not include any flexibility, it did not have a pole/zero frequency response necessary for the optimal algorithm. A structural sensor was used in the feedback loop, and the optimal PPF filters were designed with the pole/zero identification algorithm. The closed-loop results showed similar success in adding damping to the structure as in the plate experiment, but the payload motion was increased from the open-loop case. This phenomenon was analyzed using the equations for the closed-loop disturbance-to-performance transfer function and by studying a simple model of the structure-motor-payload interaction. To damp the vibration in the structure, the motor slewed the payload in the fashion of a tuned vibration absorber. The optimal algorithm was shown to be effective at vibration suppression, but ineffective at vibration isolation of a rigid slewing body.

5.1 Recommendations and Future Work

There is much future work needed on the optimal PPF design algorithm to make it applicable to real-world structural control problems. First, the pole/zero identification routine must be further developed to identify multiple pole/zero ratios over the

entire frequency spectrum in one frequency sweep. Currently, it can only identify one pole and one zero at a time and must be manually re-run for each PPF filter design. The ability of the pole/zero identification routine to identify highly damped poles and zeros also needs to be studied. The coupling effect of multiple PPF filters must be analyzed in greater detail. Further analysis may reveal more PPF design criteria based on modal frequency ratios as well. The algorithm must also be updated to design the gain of the PPF filters as well as the damping and frequency. A more sophisticated identification routine may be necessary to design the PPF gain based on gain and phase margins of the loop transfer function. In general, the on-line optimal PPF algorithm needs to be refined into a seamless algorithm that can design several PPF filters completely autonomously. The other possible use of the optimal algorithm that could be analyzed is with a multiple-input, multiple output (MIMO) control system. A structure having multiple actuators and sensors could yield better results by using the optimal PPF algorithm in a MIMO configuration than with several independent SISO control loops. The optimal PPF algorithm could also be used adaptively for a structure with time-varying dynamics by re-running it often enough to identify the changes in the pole and zero frequencies. The results from the MACE-II reflight will shed some light on the ability of the algorithm to perform adaptively.

Bibliography

Balas, M., 1978, “Active Control of Flexible Systems,” *Journal of Optimization Theory and Applications*, Vol. 25, No. 3, pp. 425–436.

Baz, A., Poh, S., and Fedor, J., 1992, “Independent Modal Space Control With Positive Position Feedback,” *Journal of Dynamic Systems, Measurement, and Control*, Vol. 114, No. 3, pp. 96–103.

Best, R., 1984, *Phase-Locked Loops*, McGraw-Hill.

Davidson, R., 1990, “Compensation of Controller-Structure Interaction Using Adaptive Residual Mode Filters,” Ph.D. Thesis, University of Colorado, Boulder, Colorado.

Dosch, J., Leo, D., and Inman, D., 1995, “Modeling and Control for Vibration Suppression of a Flexible Active Structure,” *Journal of Guidance, Control, and Dynamics*, Vol. 18, pp. 340–346.

Fagan, G. T., 1993, “An Experimental Investigation into Active Damage Control Systems Using Positive Position Feedback for AVC,” M.S. Thesis, Virginia Polytechnic Institute and State University.

Fanson, J. and Caughey, T., 1990, “Positive Position Feedback Control for Large Space Structures,” *AIAA Journal*, Vol. 28, No. 4, pp. 717–724.

Gevarter, W., 1970, “Basic Relations for Control of Flexible Vehicles,” *AIAA Journal*, Vol. 8, No. 4, pp. 666–672.

- Inman, D., 1996, *Engineering Vibration*, Prentice Hall.
- James, M., Smith, G., Wolford, J., and Whaley, P., 1989, *Vibration of Mechanical and Structural Systems: With Microcomputer Applications*, Harper and Row.
- Leo, D., 1997, "Microcontroller-Based Implementation of Adaptive Structural Control," *Final Report, Summer Faculty Research Program, Phillips Laboratory*.
- Leo, D. and Griffin, S., 1998, "Microcontroller-Based Implementation of Active Noise and Vibration Control," *SPIE Proceedings of the Fifth Annual Symposium on Smart Structures and Materials*, Vol. 3329, pp. 115–127.
- Lu, J., 1999, "Broadband Noise Reduction Using Digital Phase-Locked Loop," M.S. Thesis, The University of Toledo.
- Martin, G., 1978, "On the Control of Flexible Mechanical Systems," Ph.D. Thesis, Stanford University.
- Miu, D. and Yang, B., 1994, "On Transfer Function Zeros of General Colocated Control Systems with Mechanical Flexibilities," *Journal of Dynamic Systems, Measurement, and Control*, Vol. 116, pp. 151–154.
- Niezrecki, C. and Cudney, H., 1997, "Structural Control Using Analog Phase-Locked-Loops," *Journal of Vibration and Acoustics*, Vol. 119, No. 1, pp. 104–109.

Appendix A

MATLAB code for optimal PPF design based on pole/zero spacing

```
% colloc.m simulates the collocated actuator/sensor transfer function
% with one pole and one zero, then uses PPF to find the relationship
% between the pole/zero spacing and the optimal PPF parameters

% collocated transfer function
clear all;
count = 1;
wz = 2*pi*380;
wp = 2*pi*260;
zeta1 = 0.01;
hold off;
wpz(count) = wz/wp;
g = 0.04/wpz(count)^2;
zeta_cl(count) = real(sqrt(((1-g)/(1-g*wpz(count)^2)-1.01)/4));

wfp = sqrt(1/(1-g*wpz(count)^2));
const = 4*zeta_cl(count)^2-(wfp^2*(1-g)+1);
alphan = roots([1,const,1]);
alpha = max(alphan);
zeta_f = zeta_cl(count)*(1/sqrt(alpha)*(1+alpha))/wfp;

wp2 = 2*pi*10;
%numc = wp2^2*[1 0 wz^2];
%denc = conv([1 2*zeta1*wp wp^2],[1 2*zeta1*wp2 wp2^2]);
numc = [1 0 wz^2];
denc = [1 2*zeta1*wp wp^2];
Gc = tf(numc,denc);
```

```

% disturbance transfer function
%numd = [wp^2*wp2^2];
numd = wp^2;
dend = denc;
Gd = tf(numd,dend);
w = linspace(0.1*2*pi,1000*2*pi,10000);
[mo,po,w] = bode(Gd,w);
%semilogx(w/2/pi,20*log10(mo(:)));
%plot(w/2/pi,20*log10(mo(:)/1E3),'r');
hold on;

% PPF filter
wf = wfp*wp;
nump = [g*wf^2];
denp = [1 2*zetaf*wf wf^2];
ppf = tf(nump,denp);

% open-loop transfer function
Gol = series(Gc,ppf);

% closed-loop transfer function
numcl = conv(numd,denp);
dencl = conv(dend,denp) - [0,0,[conv(nump,numc)]];
Gcl = tf(numcl,dencl);
[mc,pc,w] = bode(Gcl,w);
%semilogx(w/2/pi,20*log10(mc(:)));
plot(w/2/pi,20*log10(mc(:)/1E3),'r');
%axis([1 6 -30 50]);
%title(['{\zeta_1} = ',num2str(zeta1)]);
%poles = pole(Gcl);
%if (wftrue/wf) >= 1
% damping(count) = -real(poles(2))/abs(poles(2));
%else
% damping(count) = -real(poles(3))/abs(poles(3));
%end
%count = count+1;
%pause

grid
%figure
%wf = 0.9*wfp*wp:0.01*wfp*wp:1.1*wfp*wp;
%plot((wf-wftrue)./wftrue*100,(zeta_cl-damping)./zeta_cl*100);

%pole(Gcl)
%j*wp*roots([1, -2*zetaf*wfp*j, -wfp^2*(1-g)-1,
2*zetaf*wfp*j, wfp^2*(1-g*wpz(end)^2)])

```

Appendix B

MATLAB code to solve for optimal PPF paramters

```
% opt_param.m finds the optimal PPF parameters as a function
of pole/zero spacing

clear all;
countg = 1;
countwpz = 1;
zeta1 = 0.0;
hold off;
for wpz = 1.1:0.1:4
    for GM = 1.2:0.2:10
        if wpz <= 1
            GM = -GM;
        end;
        zeta_cl(countwpz,countg) = 0.25*(sqrt(((1-GM^(-1))*wpz^(-2))/
(1-GM^(-1)-1)));
wfp(countg) = sqrt(1/(1-GM^(-1)));
zetaf(countwpz,countg) = (zeta_cl(countwpz,countg)*2)/
wfp(countg);
countg = countg+1;
    end;
    countg = 1;
    countwpz = countwpz+1;
end;

wpz = 1.1:0.1:4;
GM = 1.2:0.2:10;
surf(wpz,GM,zetaf')
xlabel('wpz');
ylabel('GM');
zlabel('zetaf');
figure;
```



```
plot(GM,wfp);;  
xlabel('GM');  
ylabel('wfp');
```

Appendix C

MATLAB code to initialize control algorithm

```
% 11/22/99
% this initializes the variables used in total_adapt and
% plate_exp adaptive routines
clear all;
%optimal PPF paramaters

opt_zetaf = [1.00E-01 2.72E+00
1.10E-01 2.47E+00 1.51E+00 2.05E-01
1.20E-01 2.27E+00 1.52E+00 2.06E-01
1.30E-01 2.09E+00 1.53E+00 2.07E-01
1.40E-01 1.94E+00 1.54E+00 2.08E-01
1.50E-01 1.81E+00 1.55E+00 2.09E-01
1.60E-01 1.69E+00 1.56E+00 2.10E-01
1.70E-01 1.59E+00 1.57E+00 2.11E-01
1.80E-01 1.50E+00 1.58E+00 2.12E-01
1.90E-01 1.42E+00 1.59E+00 2.13E-01
2.00E-01 1.34E+00 1.60E+00 2.14E-01
2.10E-01 1.28E+00 1.61E+00 2.15E-01
2.20E-01 1.21E+00 1.62E+00 2.15E-01
2.30E-01 1.16E+00 1.63E+00 2.16E-01
2.40E-01 1.11E+00 1.64E+00 2.17E-01
2.50E-01 1.06E+00 1.65E+00 2.18E-01
2.60E-01 1.02E+00 1.66E+00 2.19E-01
2.70E-01 9.77E-01 1.67E+00 2.19E-01
2.80E-01 9.39E-01 1.68E+00 2.20E-01
2.90E-01 9.04E-01 1.69E+00 2.21E-01
3.00E-01 8.71E-01 1.70E+00 2.21E-01
3.10E-01 8.40E-01 1.71E+00 2.22E-01
3.20E-01 8.11E-01 1.72E+00 2.23E-01
3.30E-01 7.83E-01 1.73E+00 2.23E-01
3.40E-01 7.57E-01 1.74E+00 2.24E-01
3.50E-01 7.33E-01 1.75E+00 2.25E-01
```

3.60E-01 7.10E-01 1.76E+00 2.25E-01
3.70E-01 6.88E-01 1.77E+00 2.26E-01
3.80E-01 6.67E-01 1.78E+00 2.27E-01
3.90E-01 6.47E-01 1.79E+00 2.27E-01
4.00E-01 6.27E-01 1.80E+00 2.28E-01
4.10E-01 6.09E-01 1.81E+00 2.28E-01
4.20E-01 5.92E-01 1.82E+00 2.29E-01
4.30E-01 5.75E-01 1.83E+00 2.29E-01
4.40E-01 5.59E-01 1.84E+00 2.30E-01
4.50E-01 5.43E-01 1.85E+00 2.30E-01
4.60E-01 5.29E-01 1.86E+00 2.31E-01
4.70E-01 5.14E-01 1.87E+00 2.31E-01
4.80E-01 5.01E-01 1.88E+00 2.32E-01
4.90E-01 4.87E-01 1.89E+00 2.32E-01
5.00E-01 4.74E-01 1.90E+00 2.33E-01
5.10E-01 4.62E-01 1.91E+00 2.33E-01
5.20E-01 4.50E-01 1.92E+00 2.34E-01
5.30E-01 4.38E-01 1.93E+00 2.34E-01
5.40E-01 4.27E-01 1.94E+00 2.35E-01
5.50E-01 4.16E-01 1.95E+00 2.35E-01
5.60E-01 4.05E-01 1.96E+00 2.36E-01
5.70E-01 3.95E-01 1.97E+00 2.36E-01
5.80E-01 3.85E-01 1.98E+00 2.36E-01
5.90E-01 3.75E-01 1.99E+00 2.37E-01
6.00E-01 3.65E-01 2.00E+00 2.37E-01
6.10E-01 3.56E-01 2.01E+00 2.38E-01
6.20E-01 3.47E-01 2.02E+00 2.38E-01
6.30E-01 3.38E-01 2.03E+00 2.38E-01
6.40E-01 3.29E-01 2.04E+00 2.39E-01
6.50E-01 3.20E-01 2.05E+00 2.39E-01
6.60E-01 3.12E-01 2.06E+00 2.39E-01
6.70E-01 3.03E-01 2.07E+00 2.40E-01
6.80E-01 2.95E-01 2.08E+00 2.40E-01
6.90E-01 2.87E-01 2.09E+00 2.40E-01
7.00E-01 2.79E-01 2.10E+00 2.41E-01
7.10E-01 2.72E-01 2.11E+00 2.41E-01
7.20E-01 2.64E-01 2.12E+00 2.41E-01
7.30E-01 2.56E-01 2.13E+00 2.42E-01
7.40E-01 2.49E-01 2.14E+00 2.42E-01
7.50E-01 2.42E-01 2.15E+00 2.42E-01
7.60E-01 2.34E-01 2.16E+00 2.43E-01
7.70E-01 2.27E-01 2.17E+00 2.43E-01
7.80E-01 2.20E-01 2.18E+00 2.43E-01
7.90E-01 2.13E-01 2.19E+00 2.44E-01
8.00E-01 2.05E-01 2.20E+00 2.44E-01
8.10E-01 1.98E-01 2.21E+00 2.44E-01
8.20E-01 1.91E-01 2.22E+00 2.45E-01

8.30E-01 1.84E-01 2.23E+00 2.45E-01
8.40E-01 1.77E-01 2.24E+00 2.45E-01
8.50E-01 1.70E-01 2.25E+00 2.45E-01
8.60E-01 1.62E-01 2.26E+00 2.46E-01
8.70E-01 1.55E-01 2.27E+00 2.46E-01
8.80E-01 1.48E-01 2.28E+00 2.46E-01
8.90E-01 1.40E-01 2.29E+00 2.46E-01
9.00E-01 1.33E-01 2.30E+00 2.47E-01
9.10E-01 1.25E-01 2.31E+00 2.47E-01
9.20E-01 1.17E-01 2.32E+00 2.47E-01
9.30E-01 1.08E-01 2.33E+00 2.47E-01
9.40E-01 9.94E-02 2.34E+00 2.48E-01
9.50E-01 9.00E-02 2.35E+00 2.48E-01
9.60E-01 7.99E-02 2.36E+00 2.48E-01
9.70E-01 6.86E-02 2.37E+00 2.48E-01
9.80E-01 5.56E-02 2.38E+00 2.49E-01
9.90E-01 3.90E-02 2.39E+00 2.49E-01
1.00E+00 0.00E+00 2.40E+00 2.49E-01
1.01E+00 3.84E-02 2.41E+00 2.49E-01
1.02E+00 5.40E-02 2.42E+00 2.49E-01
1.03E+00 6.56E-02 2.43E+00 2.50E-01
1.04E+00 7.52E-02 2.44E+00 2.50E-01
1.05E+00 8.35E-02 2.45E+00 2.50E-01
1.06E+00 9.08E-02 2.46E+00 2.50E-01
1.07E+00 9.74E-02 2.47E+00 2.50E-01
1.08E+00 1.03E-01 2.48E+00 2.51E-01
1.09E+00 1.09E-01 2.49E+00 2.51E-01
1.10E+00 1.14E-01 2.50E+00 2.51E-01
1.11E+00 1.19E-01 2.51E+00 2.51E-01
1.12E+00 1.23E-01 2.52E+00 2.51E-01
1.13E+00 1.28E-01 2.53E+00 2.52E-01
1.14E+00 1.31E-01 2.54E+00 2.52E-01
1.15E+00 1.35E-01 2.55E+00 2.52E-01
1.16E+00 1.39E-01 2.56E+00 2.52E-01
1.17E+00 1.42E-01 2.57E+00 2.52E-01
1.18E+00 1.45E-01 2.58E+00 2.52E-01
1.19E+00 1.48E-01 2.59E+00 2.53E-01
1.20E+00 1.51E-01 2.60E+00 2.53E-01
1.21E+00 1.54E-01 2.61E+00 2.53E-01
1.22E+00 1.57E-01 2.62E+00 2.53E-01
1.23E+00 1.59E-01 2.63E+00 2.53E-01
1.24E+00 1.62E-01 2.64E+00 2.53E-01
1.25E+00 1.64E-01 2.65E+00 2.54E-01
1.26E+00 1.67E-01 2.66E+00 2.54E-01
1.27E+00 1.69E-01 2.67E+00 2.54E-01
1.28E+00 1.71E-01 2.68E+00 2.54E-01
1.29E+00 1.73E-01 2.69E+00 2.54E-01

```

1.30E+00 1.75E-01 2.70E+00 2.54E-01
1.31E+00 1.77E-01 2.71E+00 2.55E-01
1.32E+00 1.79E-01 2.72E+00 2.55E-01
1.33E+00 1.81E-01 2.73E+00 2.55E-01
1.34E+00 1.82E-01 2.74E+00 2.55E-01
1.35E+00 1.84E-01 2.75E+00 2.55E-01
1.36E+00 1.86E-01 2.76E+00 2.55E-01
1.37E+00 1.87E-01 2.77E+00 2.55E-01
1.38E+00 1.89E-01 2.78E+00 2.56E-01
1.39E+00 1.90E-01 2.79E+00 2.56E-01
1.40E+00 1.92E-01 2.80E+00 2.56E-01
1.41E+00 1.93E-01 2.81E+00 2.56E-01
1.42E+00 1.94E-01 2.82E+00 2.56E-01
1.43E+00 1.96E-01 2.83E+00 2.56E-01
1.44E+00 1.97E-01 2.84E+00 2.56E-01
1.45E+00 1.98E-01 2.85E+00 2.56E-01
1.46E+00 2.00E-01 2.86E+00 2.57E-01
1.47E+00 2.01E-01 2.87E+00 2.57E-01
1.48E+00 2.02E-01 2.88E+00 2.57E-01
1.49E+00 2.03E-01 2.89E+00 2.57E-01
1.50E+00 2.04E-01 2.90E+00 2.57E-01
];

```

```

T = 1/15000;
zetaf = opt_zetaf(:,2);
wpz = opt_zetaf(:,1);
g = 1;

%integrator (double w/ zero bias)

zero_freq = 0;
pole1 = 2*pi*5;
pole2 = 2*pi*5;
pole3 = 2*pi*5;
cfilt = tf([1 zero_freq],conv(conv([1 pole1],[1 pole2]),[1 pole3]));
dfilt = c2d(cfilt,T);
[numd,dend] = tfdata(dfilt,'v');

%zero-bias prefilter to pole/zero routine
prefiltc = tf([1 0],[1 2*pi*1000]);
prefiltd = c2d(prefiltc,T);
[prenum,predden] = tfdata(prefiltd,'v');

% lowpass filter for pole/zero routine
lowpassc = tf([4*pi^2*100^2],conv([1 2*pi*100],[1 2*pi*100]));
lowpassd = c2d(lowpassc,T);

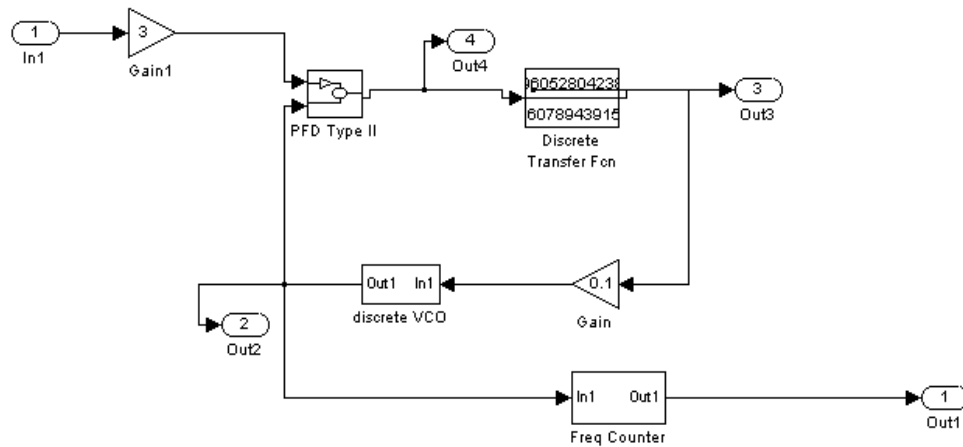
```

```
[lownum,lowden] = tfdata(lowpassd,'v');

% frequency sweep routine
start_freq = 400;      %(Hz)
end_freq = 700;
tend = 20;
p = 2; %quadratic chirp
beta = (end_freq-start_freq).*(tend.^(-p));
```

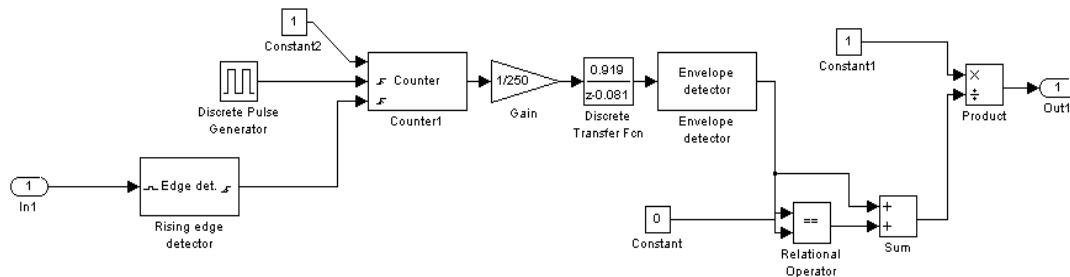
Appendix D

SIMULINK diagram of digital phase-locked loop



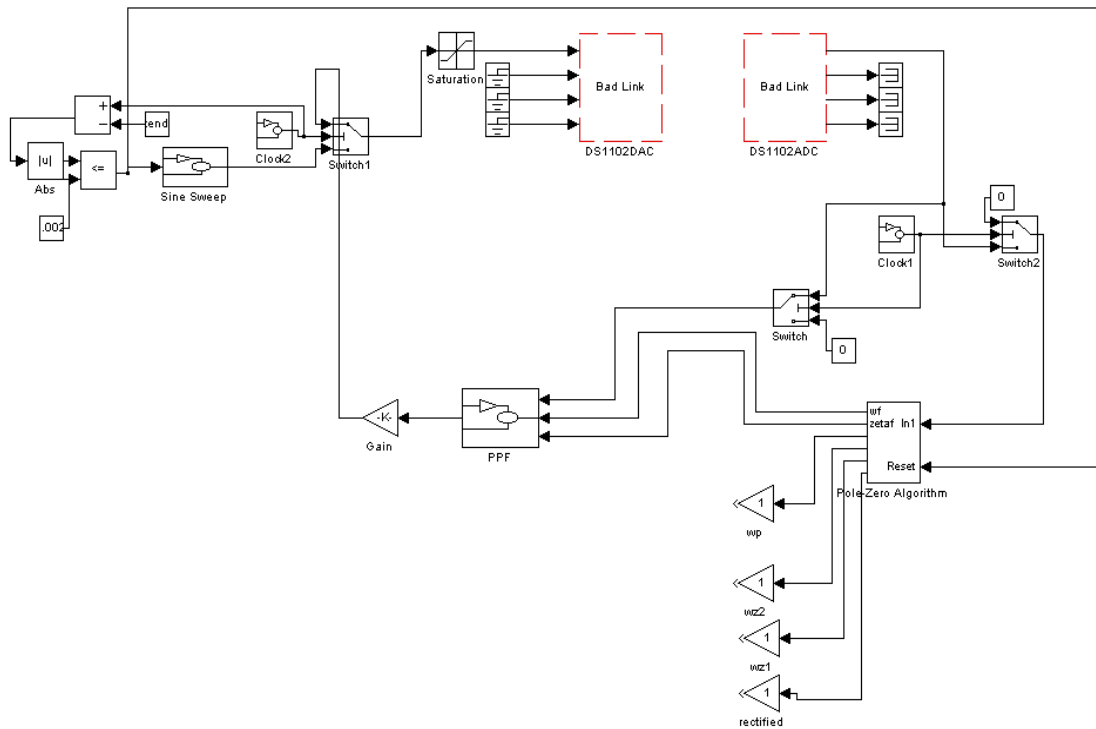
Appendix E

SIMULINK diagram of frequency detector



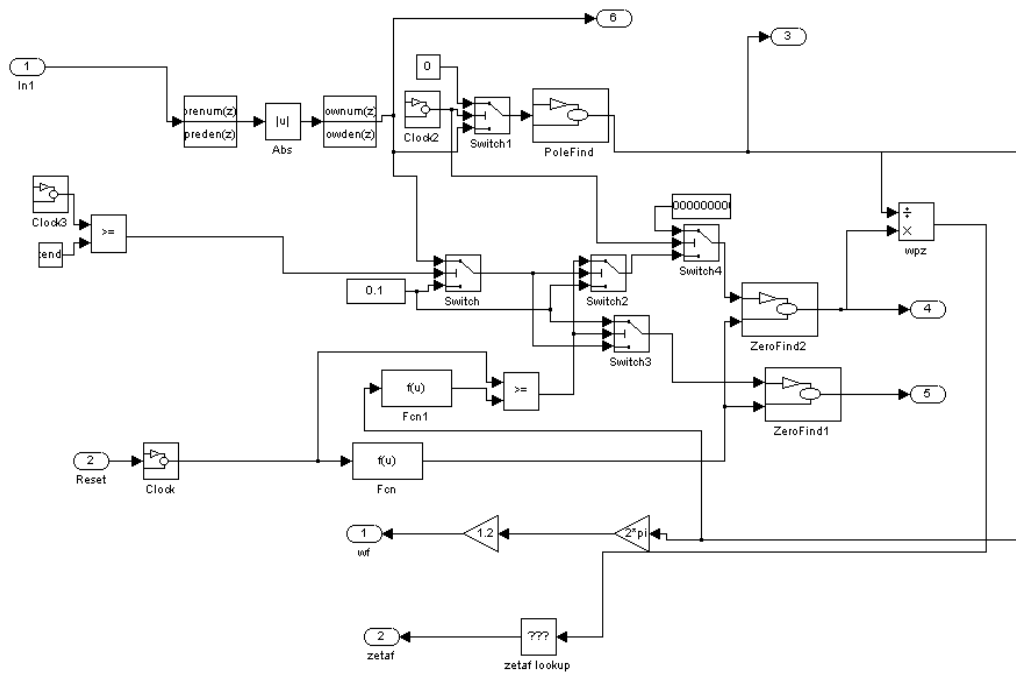
Appendix F

SIMULINK diagram of on-line control algorithm



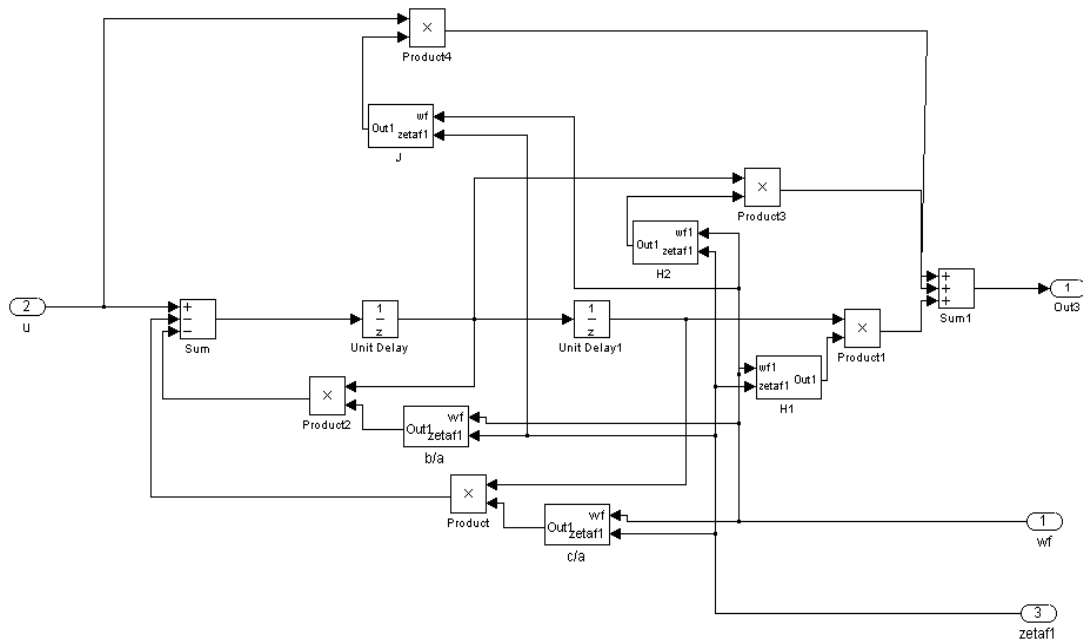
Appendix G

SIMULINK diagram of pole/zero identification routine



Appendix H

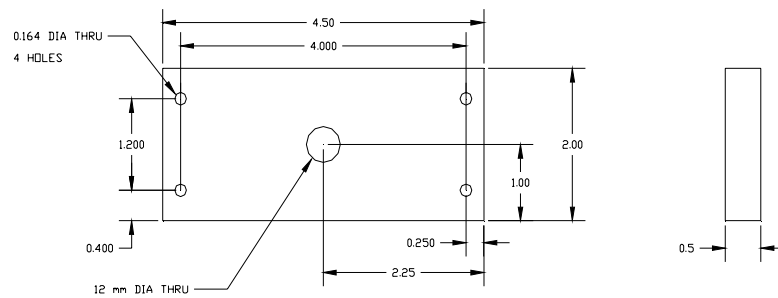
SIMULINK model of PPF filter



Appendix I

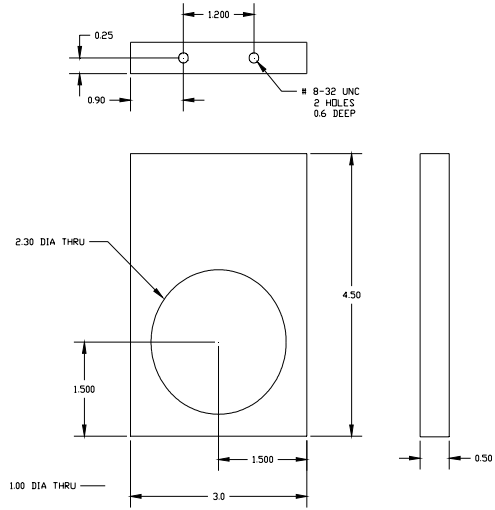
Mini-MACE schematics

MOTOR ATTACHMENT PLATE



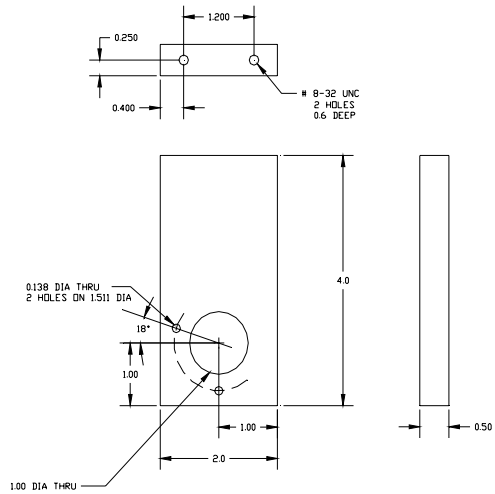
ALL DIMENSIONS SHOWN IN INCHES
UNLESS OTHERWISE NOTED

MOTOR PLATE - ENCODER SIDE



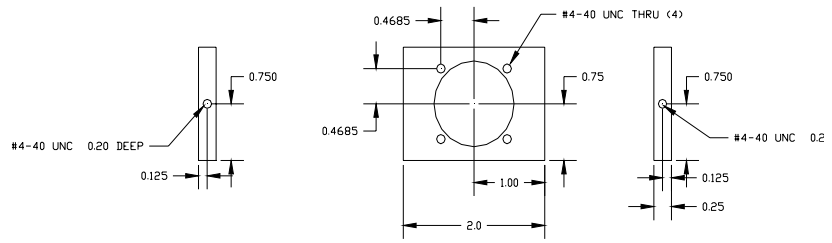
ALL DIMENSIONS SHOWN IN INCHES

MOTOR PLATE - PAYLOAD SIDE



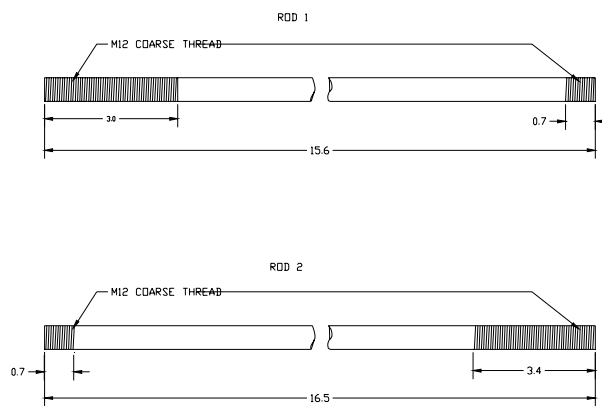
ALL DIMENSIONS SHOWN IN INCHES

TACHOMETER MOUNT



ALL DIMENSIONS SHOWN IN INCHES

0.5 IN DIA RODS



ALL DIMENSIONS SHOWN IN INCHES UNLESS OTHERWISE NOTED

Vita

The author, Mark Andrew McEver, son of Dr. William S. and Victoria W. McEver, was born on November 12, 1976, in Alexandria, Virginia. He obtained his high school diploma from Fauquier High School, in Warrenton, Virginia, in 1994. He then went to Virginia Polytechnic Institute and State University, in Blacksburg, Virginia, where he earned a Bachelor of Science in Mechanical Engineering in 1998. Staying at Virginia Tech another year and a half, he pursued a Master of Science degree concentrating on vibrations and controls. He will attend Duke University in Spring 2000 to pursue a doctoral degree in mechanical engineering.

Permanent Address: 7079 Lakeview Drive
Warrenton, Virginia 20187

This thesis was typeset with L^AT_EX 2_ε¹ by the author.

¹L^AT_EX 2_ε is an extension of L^AT_EX. L^AT_EX is a collection of macros for T_EX. T_EX is a trademark of the American Mathematical Society. The macros used in formatting this thesis were written by Greg Walker, Department of Mechanical Engineering, Virginia Tech.